Electronic Supplementary Information

High-Efficiency Electrosynthesis of Urea over Bacterial Cellulose Regulated Pd-Cu Bimetallic Catalyst

Shengbo Zhang,[†ab] Jing Geng,[†ab] Zhong Zhao,[ab] Meng Jin,[ab] Wenyi Li,[ab] Yixing Ye,[ab] Ke Li,*[c] Guozhong Wang,[ab] Yunxia Zhang,[ab] Huajie Yin,[ab] Haimin Zhang,*[ab] and Huijun Zhao[d]

[a.] *Key Laboratory of Materials Physics, Centre for Environmental and Energy Nanomaterials, Anhui Key Laboratory of Nanomaterials and Nanotechnology, CAS Center for Excellence in Nanoscience, Institute of Solid State Physics, Chinese Academy of Sciences, Hefei 230031, China. E-mail:* zhanghm@issp.ac.cn

[b.] *University of Science and Technology of China, Hefei 230026, China*

[c.] *Key Laboratory of Agricultural Sensors, Ministry of Agriculture, School of Information and Computer, Anhui Agricultural University, Hefei 230026, China. E-mail:* kelee@ustc.edu.cn

[d.] *Center for Catalysis and Clean Energy, Griffith University, Gold Coast Campus, QLD4222, Australia*

[†] *These authors contributed equally to this work*

Experimental Section

Methods

Reagents and materials. Bacterial cellulose (BC) pellicle was obtained from Guilin Qihong Technology Co., Ltd., China. $PdCl_2$ and $CuSO_4{\cdot}5H_2O$ were purchased from Sinopharm Chemical Reagent Co., Ltd. KNO_3 (99.0%), sodium nitroferricyanide(III) dehydrate ($C_5FeN_6Na_2O{\cdot}2H_2O$, 99.0%), sodium citrate ($C_6H_5Na_3O_7{\cdot}2H_2O$, 99.0%), NaOH (96.0%), salicylic acid ($C_7H_6O_3$, 99.5%), NaClO (available chlorine ≥ 5.0%), NH_4Cl (99.5%), $C_9H_{11}NO$ (99.0%), H_3PO_4 (≥ 85%), H_2SO_4 (≥ 85%), $FeCl_3$ (99.9%), diacetylmonoxime ($C_4H_7NO_2$, AR), thiosemicarbazide (CH_5N_3S, 99.0%), *p*-aminobenzenesuifonamide ($NH_2C_6H_4SO_2NH_2$, 95.0%), N-(1-naphthyl) ethylenediamine dihydrochloride ($C_{10}H_7NHC_2H_4NH_2{\cdot}2HCl$, 95.0%), $^{15}KNO_3$ (AR), $^{14}NH_2CO^{14}NH_2$ (AR), $^{15}NH_2CO^{15}NH_2$ (AR), were purchased from Aladdin. All solutions were prepared using deionized water (Millipore Corp., 18.2 MΩ cm). Commercial carbon paper (CP, HCP030N) was purchased from Shanghai Hesen Electric Co. Ltd.

Fabrication of PdCu/CBC. BC pellicle was firstly frozen by liquid nitrogen and freeze-dried in a bulk tray dryer at a sublimating temperature of −75 °C and a pressure of 0.01 mbar for 48 h. To remove possible organic contaminations, the freeze-dried BC was dispersed in 200 mL of piranha solution under constant stirring at room temperature for 6 h, thoroughly washed with deionized water and freeze-dried again. The pre-treated BC (1.0 g) was immersed in a 200 mL of solution containing 1.0 mmol Pd^{2+} (concentration of Pd^{2+}: 5.0 mmol L^{-1}) and 0.5 mmol Cu^{2+} (concentration of Cu^{2+}: 2.5 mmol L^{-1}) for 6 h. The obtained sample were adequately washed with the Millipore water, freeze-dried and carbonised in a tubular furnace

under an Ar atmosphere. The sample was firstly heated to 360 °C with a heating rate of 2 °C min^{-1} and kept for 2 h, then heated to 700 °C with a heating rate of 5 °C min^{-1} and kept for 3 h to carbothermally reduce the adsorbed Pd^{2+} and Cu^{2+} on BC to metallic PdCu alloying nanoparticles, and simultaneously carbonize BC into graphitic carbon (denoted as PdCu/CBC). Pd/CBC sample with Pd^{2+} concentration of 7.5 mmol L^{-1} and Cu/CBC sample with Cu^{2+} concentration of 7.5 mmol L^{-1} were also fabricated utilizing the same procedure as PdCu/CBC sample. The resultant PdCu/CBC, Pd/CBC and Cu/CBC samples were adequately washed with deionized water and ethanol, and dried at 60 °C under vacuum for 6 h.

Characterization. XRD patterns were acquired using Philips X'pert PRO with Nifiltered monochromatic CuKa radiation (λKα1=1.5418 Å) at 40 kV and 40 mA. FT-IR spectra were measured by a Nicolet Nexus FT-IR spectrometer with KBr pellet technique ranging from 400 to 4000 cm^{-1} at room temperature. SEM images were obtained using SU8020 (Hitachi, Japan) with a field emission scanning electron microanalyzer at an acceleration voltage of 10.0 kV. TEM images were obtained using JEMARM 200F operating at an accelerating voltage of 200 kV. XPS measurements were performed on an ESCALAB 250 X-ray photoelectron spectrometer (Thermo, America) equipped with Al Kα1, 2 monochromatized radiations at 1486.6 eV X ray source. The Pd and Cu contents were quantitatively determined by the ICP-AES (ICP-6300, Thermo Fisher Scientific). Nitrogen adsorption-desorption isotherms were measured using an automated gas sorption analyzer (Autosorb-iQ-Cx).

Operando SR-FTIR measurement. The *operando* SR-FTIR measurements were conducted at the infrared beamline BL01B of the National Synchrotron Radiation Laboratory through a homemade top-plate cell-reflection infrared set-up with a ZnSe crystal as the infrared

transmission window (cut-off energy of ~625 cm^{-1}).[1] This end station was equipped with an FTIR spectrometer (Bruker 70 v/s) with a KBr beam splitter and various detectors (herein, a liquid-nitrogen-cooled mercury cadmium telluride detector was used) coupled with an infrared microscope (Bruker Hyperion 2000) with an × 15 objective. The catalyst electrode was tightly pressed against the ZnSe crystal window with a micrometre-scale gap to reduce the loss of infrared light.[1] To ensure the quality of the obtained SR-FTIR spectra, the apparatus adopted a reflection mode with a vertical incidence of infrared light. Each infrared absorption spectrum was acquired by averaging 128 scans at a resolution of 4 cm^{-1}.[1] The measured potential ranges of the electrocatalytic oxidation reaction were −0.20 to −0.70 V (*vs.* RHE) with an interval of 0.10 V. The *operando* electrochemical set-up is shown in **Fig. S28**.

Operando Raman measurements. For the *operando* Raman tests, the samples were recorded on a RXN1-785 Raman spectrometer (Analytik Jena AG, excited wavelength of 785 nm) connected with CHI 660 E electrochemical workstation. The *operando* electrochemical set-up is shown in **Fig. S29**.

Electrochemical measurements. All electrochemical measurements were performed on a CHI 760E electrochemical workstation (CH Instrumental Corporation, Shanghai, China) under ambient conditions using a Nafion 211 proton exchange membrane separated two-compartment H-type electrochemical cell accommodated 50 mL of CO_2-saturated 0.05 M KNO_3 electrolyte in each compartment and a three-electrode electrochemical system with a PdCu/CBC working electrode, an Ag/AgCl (Saturated KCl) reference electrode and a Pt mesh counter electrode. Prior to use, the Nafion 211 membrane was treated by successive heating at 80 °C in H_2O_2 (5.0 wt.%) aqueous solution for 1 h and in deionized water for

another 1 h. The working electrode was prepared as follows: 2.5 mg of the targeted electrocatalyst was firstly dispersed in 95 μL of absolute ethanol and 5.0 μL of Nafion solution (5.0 wt.%) under sonication for 30 min to form a homogeneous ink. 10 μL of ink was loaded onto carbon paper electrode (1×1 cm^2, equivalent to 0.25 mg cm^{-2}) and dried under ambient conditions for 40 min before use. Before the electrocatalysis, Ar gas was persistently bubbled into the electrolyte to eliminate O_2 interference and the electrolyte was bubbled with CO_2 for 20 min. Then the purified CO_2 was continuously fed into the cathodic compartment with a constant flow rate of 20 mL min^{-1} during the experiments. The electrolyte in the cathodic compartment was stirred at a rate of 500 rpm during electrocatalysis. In this work, all measured potentials *vs.* Ag/AgCl were converted to the potentials *vs.* RHE (E_{RHE}) according to the following equation:

$$E_{RHE} = E_{Ag/AgCl} + 0.059pH + E^{\circ}_{Ag/AgCl} \quad (1)$$

where, $E_{Ag/AgCl}$ is the equilibrium potential under standard conditions, $E^{o}_{Ag/AgCl}$ = 0.1967 V *vs*. RHE at 25 ^{o}C.

Determination of urea, ammonia, nitrite and hydrazine. As-produced urea was spectrophotometrically determined by the ^{1}H NMR and urease decomposition methods.[2,3] The content of nitrite in the electrolyte was also measured by ultraviolet spectrophotometry.[4] The yielded ammonia was determined by the standard indophenol blue method.[5] The standard Watt and Chrisp method was employed to determine hydrazine.[6]

Isotope labelling experiments. For quality assurance required, ^{15}N isotopic labelling experiments were conducted using CO_2-saturated 0.05 M $K^{15}NO_3$ as the electrolyte with

identical experimental procedure as that of CO_2-saturated 0.05 M $K^{14}NO_3$ experiments. For ^1H NMR method, after electrocatalysis, the entire reaction solution in the cathode compartment was collected, adjusted to pH ~ 5.0. As a typical NMR test process, 900 μL of electrolyte was extracted, followed by the additions of 100 μL d6-DMSO (99.9 atom% D, Aladdin Biochemical Technology Co., Ltd. Shanghai) as internal standard. The yielded $^{15}NH_2CO^{15}NH_2$ and $^{14}NH_2CO^{14}NH_2$ were analyzed by the ^1H NMR and ^{13}C NMR methods using Bruker Avance-400 MHZ. The yielded $^{15}NH_2CO^{15}NH_2$ was analyzed by the ^{15}N NMR methods using Bruker Avance-400 MHZ.

Calculation of R_{urea}, R_{NH3}, R_{NO2^-} and FE. R_{urea} and FE are calculated by the following equations:

$$R_{urea}\,(\mu g\ h^{-1}\ mg_{cat.}^{-1}) = \frac{C_{urea}\,(\mu g\ mL^{-1}) \times V(mL)}{t\,(h) \times m_{cat.}\,(mg)} \quad (2)$$

$$FE\ (\%) = \frac{16 \times n_{urea}\,(mol) \times F\ (C\ mol^{-1})}{Q\ (C)} \times 100\% \quad (3)$$

where, C_{urea} and V are the measured urea concentration and the electrolyte solution volume, respectively, t is the electrolysis period and $m_{cat.}$ is the amount of the loaded electrocatalyst, F is the faradaic constant (96485 C mol^{-1}) and Q is the total charge transferred during electrolysis period.

R_{NH3} and FE are calculated by the following equations:

$$R_{NH_3}\,(\mu g\ h^{-1}\ mg_{cat.}^{-1}) = \frac{C_{NH_3}\,(\mu g\ mL^{-1}) \times V(mL)}{t\,(h) \times m_{cat.}\,(mg)} \quad (4)$$

$$FE\ (\%) = \frac{8 \times n_{NH_3}\,(mol) \times F\ (C\ mol^{-1})}{Q\ (C)} \times 100\% \quad (5)$$

where, C_{NH3} and V are the measured NH_3 concentration and the electrolyte solution volume,

respectively, t is the electrolysis period and $m_{cat.}$ is the amount of the loaded electrocatalyst, F is the faradaic constant (96485 C mol^{-1}) and Q is the total charge transferred during electrolysis period.

$R_{NO_2^-}$ and FE are calculated by the following equations:

$$R_{NO_2^-}\ (\mu g\ h^{-1}\ mg_{cat.}^{-1}) = \frac{C_{NO_2^-}\ (\mu g\ mL^{-1}) \times V(mL)}{t\ (h) \times m_{cat.}\ (mg)} \quad (6)$$

$$FE\ (\%) = \frac{2 \times n_{NO_2^-}\ (mol) \times F\ (C\ mol^{-1})}{Q\ (C)} \times 100\% \quad (7)$$

where, $C_{NO_2^-}$ and V are the measured NO_2^- concentration and the electrolyte solution volume, respectively, t is the electrolysis period and $m_{cat.}$ is the amount of the loaded electrocatalyst, F is the faradaic constant (96485 C mol^{-1}) and Q is the total charge transferred during electrolysis period.

Determination of carbon monoxide (CO) and hydrogen (H_2). The amounts of CO and H_2 were quantitatively analyzed by gas chromatography (GC) measurements.

Theoretical calculations. The first-principle calculations were performed within the framework of DFT as implemented in the Vienna Ab initio Simulation Package (VASP).[7] The projector augmented wave (PAW) method has been used to describe the inert core electrons and the Van der Waals correction (DFT-D3) was used to improve the description of the dispersion interaction between adsorbates and substrates.[8] The electronic exchange-correlation effects were described with Perdew-Burke-Ernzerhof generalized gradient approximation (PBE-GGA) functional.[9,10] A vacuum of 15 Å in the z-direction is used. The 3×3×3 supercell of PdCu was constructed and the corresponding (111) plane was cleaved to build the slab model. For the structural relaxations, the convergence criteria of 1.0

$\times 10^{-5}$ eV atom^{-1} and 0.05 eV Å^{-1} were used for the electronic self-consistent iteration and the maximum force on each atom, respectively. A cut off energy of 450 eV was used for the expansion of the wave functions. The gamma (Γ) cantered 3 × 5 × 1 Monkhorst-Pack k-point sampling was used throughout. Additionally, a vacuum thickness of 15 Å was added in the z direction of all the configurations to avoid the interaction between the adsorbate and periodic images. The adsorption free energies of reaction intermediates were calculated by using the computational hydrogen electrode model developed by Nørskov et al.[11]

Supplementary Tables and Figures

Table S1. Impregnated Pd^{2+}/Cu^{2+} contents on BC from different adsorption solutions and corresponding Pd/Cu amount loaded on CBC.

Samples	**[Pd^{2+}]/[Cu^{2+}] in Adsorption Solution** (mmol L^{-1})	**Pd/Cu in Pd/CBC, Cu/CBC, PdCu/CBC** (wt.%)	**Pd/Cu Molar Ratio in PdCu/CBC**
Pd/CBC	7.5/-	2.1/-	-
Cu/CBC	-/7.5	-/2.5	-
PdCu/CBC	5.0/2.5	1.2/0.7	1:1

Table S2. Electrocatalytic urea synthesis performance of the reported elecatalysts and PdCu/CBC.

Ref	Catalyst	Reactant	Conditions	Urea Production Rate	FE (%)	By-product
12	Pd_1Cu_1/TiO_2-400	$N_2 + CO_2$	0.1 M $KHCO_3$	3.36 mmol h^{-1} g^{-1}	8.92	CO, H_2, NH_3
13	PPy-coated Pt	$N_2 + CO_2$	0.1 M Li_2SO_4/ 0.03 M H^+	2.4 μmol h^{-1}	7.1	NH_3, HCOOH
14	$Bi/BiVO_4$	$N_2 + CO_2$	0.1 M $KHCO_3$	5.91 mmol h^{-1} g^{-1}	12.55	CO, H_2, NH_3
15	$BiFeO_3/BiVO_4$	$N_2 + CO_2$	0.1 M $KHCO_3$	4.94 mmol h^{-1} g^{-1}	17.18	CO, H_2, NH_3
16	$Ni(BO_3)_2$	$N_2 + CO_2$	0.1 M $KHCO_3$	9.70 mmol h^{-1} g^{-1}	20.36	CO, H_2, NH_3
17	Co-PMDA-2-mblM	$N_2 + CO_2$	0.1 M $KHCO_3$	14.47 mmol h^{-1} g^{-1}	48.97	CO, H_2, NH_3
18	Rice-like InOOH	$N_2 + CO_2$	0.1 M $KHCO_3$	6.85 mmol h^{-1} g^{-1}	20.97	CO, H_2, NH_3
19	Ni-Pc	$NO_2^- + CO_2$	0.2 M $KHCO_3$	-	40	CO, NH_3
20	$FeTiO_3$	$NO_2^- + CO_2$	1 M $NaHCO_3$	-	-	-
21	Cu-TiO_2	$NO_2^- + CO_2$	0.2 M $KHCO_3$	20 μmol h^{-1}	43.1	CO, H_2, N_2, NH_3
22	Te-Pd NCs	$NO_2^- + CO_2$	0.05 M KNO_2	-	12.2	CO, H_2, N_2, NH_3
23	AuCu SANFs	$NO_2^- + CO_2$	0.01 M KNO_2	3889.6 μg h^{-1} $mg_{cat.}^{-1}$	24.7	CO, H_2, N_2, NH_3
24	ZnO-V	$NO_2^- + CO_2$	0.2 M $NaHCO_3$ + 0.1 M $NaNO_2$	16.56 μmol h^{-1}	23.26	CO, H_2, NO, NH_3

25	Zn nanobelts	$NO + CO_2$	0.2 M $KHCO_3$	15.13 mmol h^{-1} g^{-1}	11.26	CO, H_2, NH_3
26	Cu-loaded gas-diffusion electrode	$NO_2^- + CO_2$	0.2 M $KHCO_3$	-	10	CO, HCOOH, NH_3
		$NO_3^- + CO_2$	0.2 M $KHCO_3$	-	35	
27	TiO_2-Nafion	$NO_3^- + CO_2$	0.1 M KNO_3	0.33 μmol h^{-1}	40	CO, H_2, NH_3
28	*V*o-InOOH	$NO_3^- + CO_2$	0.1 M KNO_3	592.5 μg h^{-1} $mg_{cat.}^{-1}$	51.0	CO, H_2, NH_3
1	$In(OH)_3$-S	$NO_3^- + CO_2$	0.1 M KNO_3	533.1 μg h^{-1} $mg_{cat.}^{-1}$	53.4	CO, H_2, NH_3
29	Cu@Zn	$NO_3^- + CO_2$	0.1 M KNO_3 + 0.2 M $KHCO_3$	7.29 μmol cm^{-2} h^{-1}	9.28	N_2, CO, H_2, NH_3, NO_2^-
3	Vo-CeO_2-750	$NO_3^- + CO_2$	0.1 M $KHCO_3$ + 50m M KNO_3	943.6 μg h^{-1} $mg_{cat.}^{-1}$	-	CO, H_2, NH_3, NO_2^-
30	Cu-GS-800	$NO_3^- + CO_2$	0.1 M K_2SO_4 + 0.1 M KNO_3	1800 μg h^{-1} $mg_{cat.}^{-1}$	28	CO, H_2 , NH_3
31	F-CNT-300	$NO_3^- + CO_2$	0.1 M KNO_3	6.36 mmol h^{-1} $g_{cat.}^{-1}$	18.0	H_2, NH_3
32	B-FeNi-DASC	$NO_3^- + CO_2$	0.1 M $KHCO_3$ + 50m M KNO_3	20.2 mmol h^{-1} $g_{cat.}^{-1}$	17.8	CO, H_2, NH_3
This work	PdCu/CBC	$NO_3^- + CO_2$	0.05 M KNO_3	763.8 ± 42.8 μg h^{-1} $mg_{cat.}^{-1}$	69.1 ± 3.8	CO, H_2, NO_2^-, NH_3
	Pd/CBC			215.1 ± 11.8 μg h^{-1} $mg_{cat.}^{-1}$	17.4 ± 1.0	
	Cu/CBC			314.2 ± 19.5 μg h^{-1} $mg_{cat.}^{-1}$	27.0 ± 1.7	

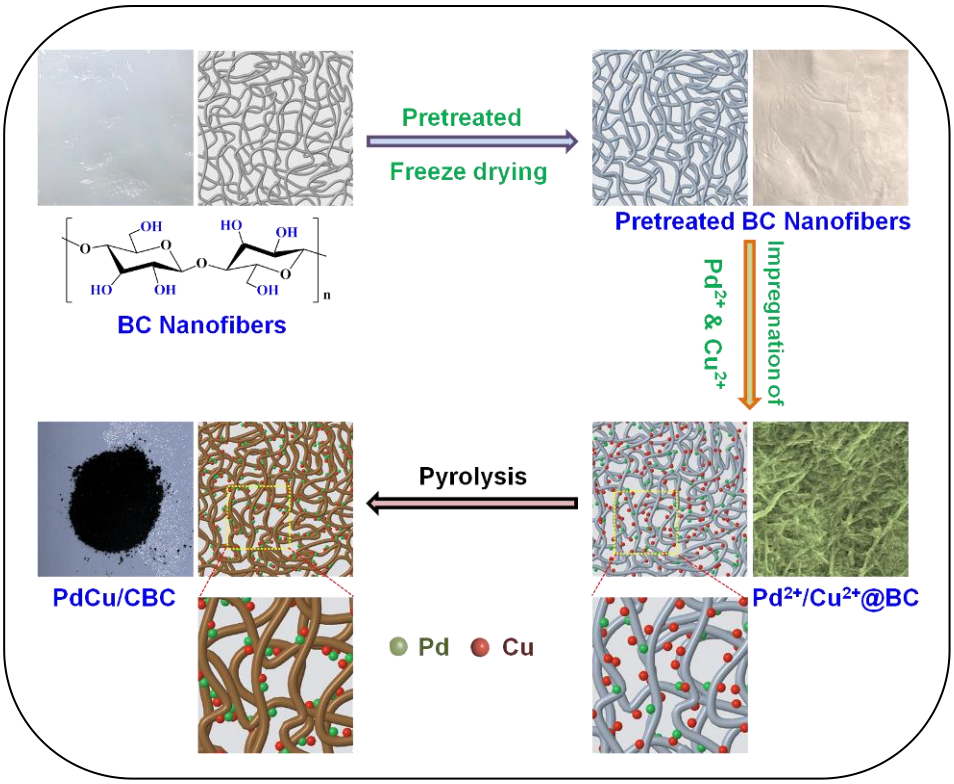

Fig. S1. Schematic illustration of the synthetic procedure of PdCu/CBC.

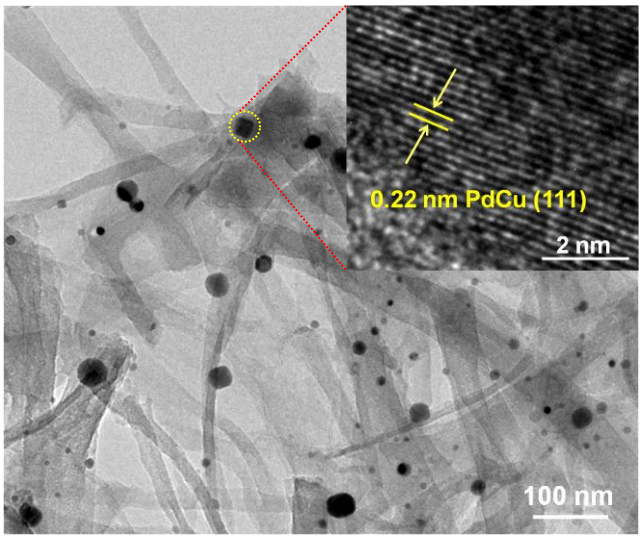

Fig. S2. TEM image obtained from different location of PdCu/CBC sample.

The transmission electron microscopy (TEM) image from different location of PdCu/CBC displays homogeneous PdCu nanoparticles loaded onto carbon support. The high-resolution TEM (HRTEM) image indicates that the lattice distance of an individual nanoparticle is 0.22 nm (inset in Figure S2), attributed to the (111) interplanar distance of PdCu alloy.

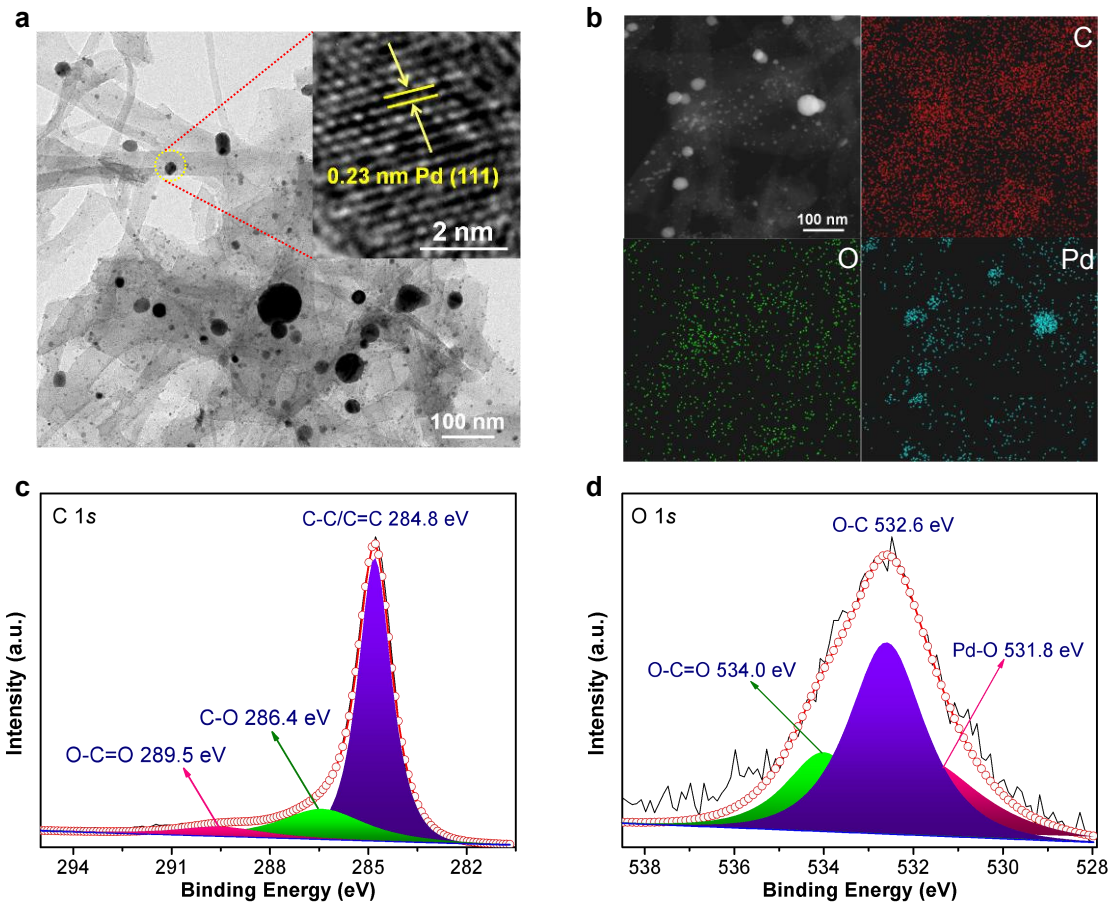

Fig. S3. (a) TEM images of Pd/CBC sample. (b) Corresponding elemental mapping images of Pd/CBC. High-resolution (c) C 1*s* and (d) O 1*s* spectra of Pd/CBC.

The transmission electron microscopy (TEM) image of Pd/CBC displays homogeneous Pd nanoparticles loaded onto carbon support (Figure S3a). The high-resolution TEM (HRTEM) image indicates that the lattice distance of an individual nanoparticle is 0.23 nm (inset in Figure S3a), attributed to the (111) interplanar distance of metallic Pd structure. The corresponding elemental mapping analysis revealed that C, O and Pd elements are homogeneously distributed over the entire Pd/CBC (Figure S3b). The high-resolution C 1s (Figure S3c) and O 1s XPS spectra (Figure S3d) confirm the presence of rich O groups and the formation of Pd-O bonds in Pd/CBC, respectively.

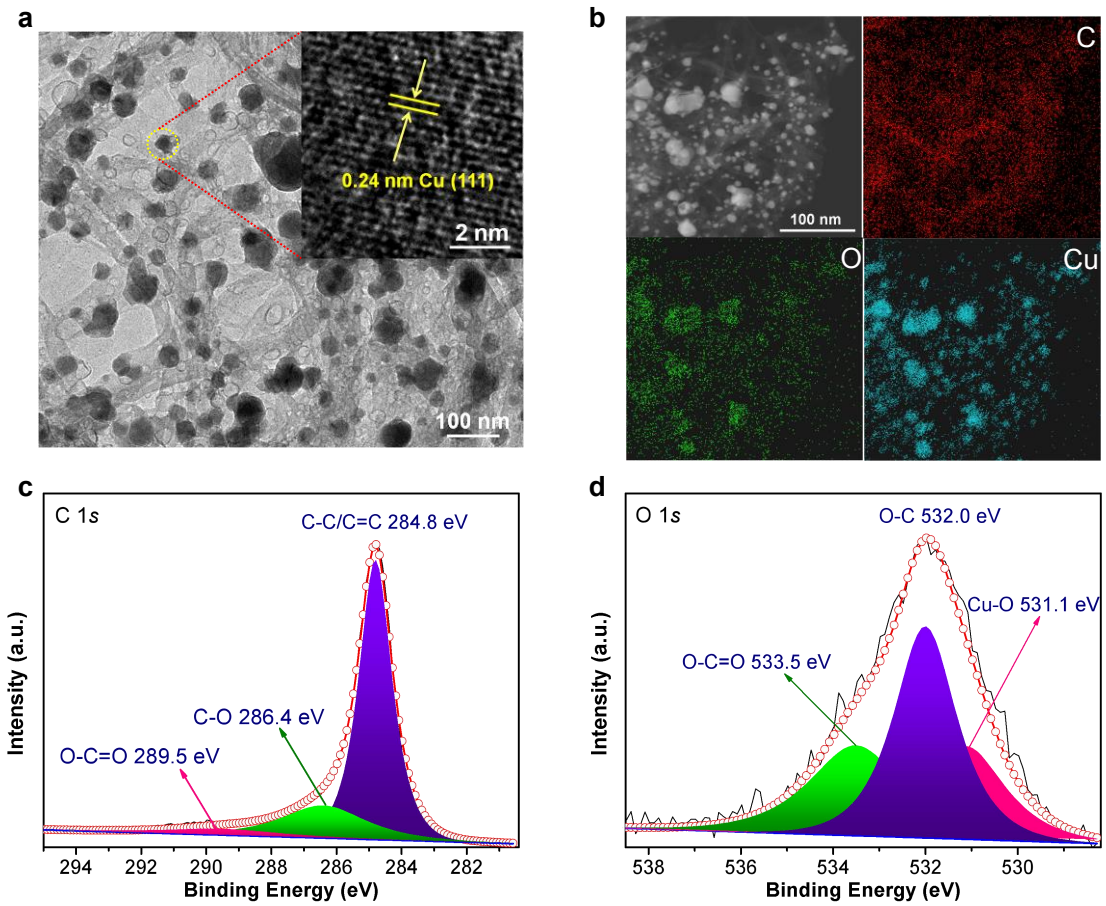

Fig. S4. (a) TEM images of Cu/CBC sample. (b) Corresponding elemental mapping images of Cu/CBC. High-resolution (c) C 1*s* and (d) O 1*s* spectra of Cu/CBC.

The transmission electron microscopy (TEM) image of Cu/CBC displays homogeneous Cu nanoparticles loaded onto carbon support (Figure S4a). The high-resolution TEM (HRTEM) image indicates that the lattice distance of an individual nanoparticle is 0.24 nm (inset in Figure S4a), attributed to the (111) interplanar distance of metallic Cu structure. The corresponding elemental mapping analysis revealed that C, O and Cu elements are homogeneously distributed over the entire Cu/CBC (Figure S4b). The high-resolution C 1s (Figure S4c) and O 1s XPS spectra (Figure S4d) confirm the presence of rich O groups and the formation of Cu-O bonds in Cu/CBC, respectively.

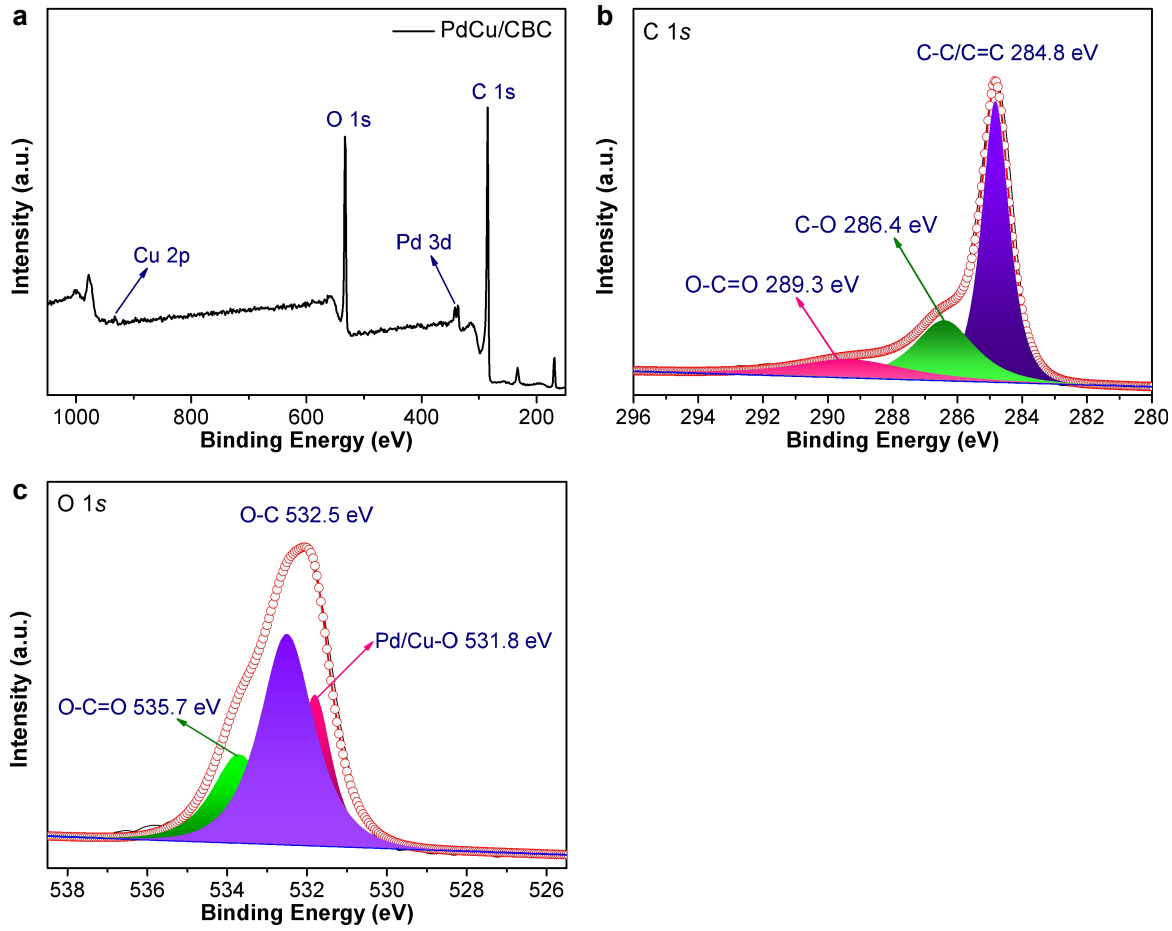

Fig. S5. (a) Surface survey XPS spectrum of PdCu/CBC. High-resolution (b) C 1*s* and (c) O 1*s* spectra of PdCu/CBC.

The X-ray photoelectron spectroscopy (XPS) survey spectrum of PdCu/CBC confirms the presence of Pd, Cu, O and C elements (Figure S5a). The high-resolution C 1s (Figure S5b) and O 1s XPS spectra (Figure S5c) confirm the presence of rich O groups and the formation of Pd/Cu-O bonds in PdCu/CBC, respectively.

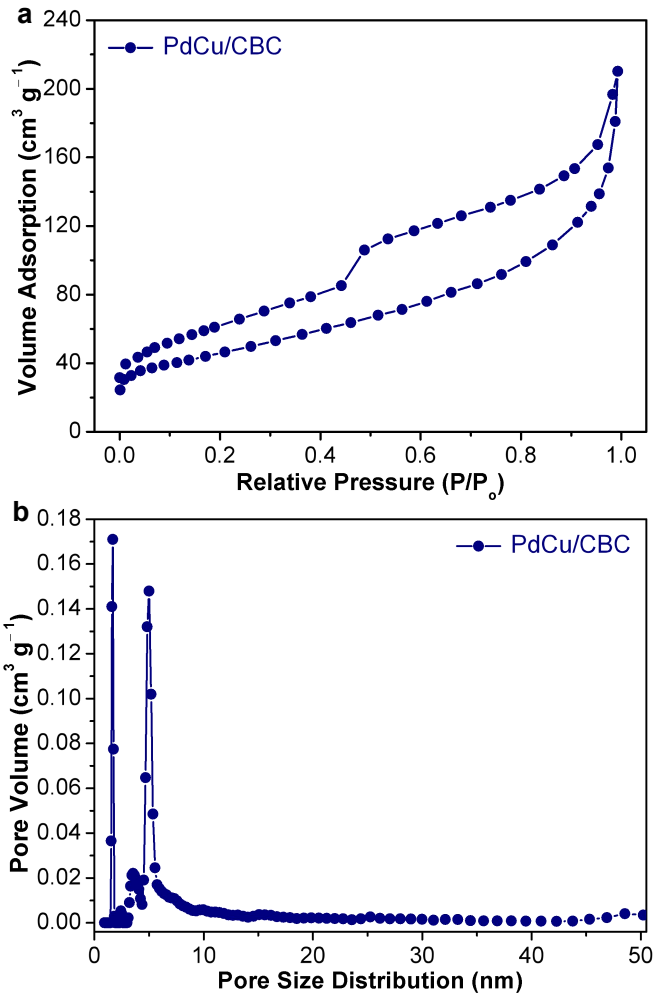

Fig. S6. (a) N_2 adsorption-desorption isotherm of PdCu/CBC. (b) Corresponding pore size distribution curve.

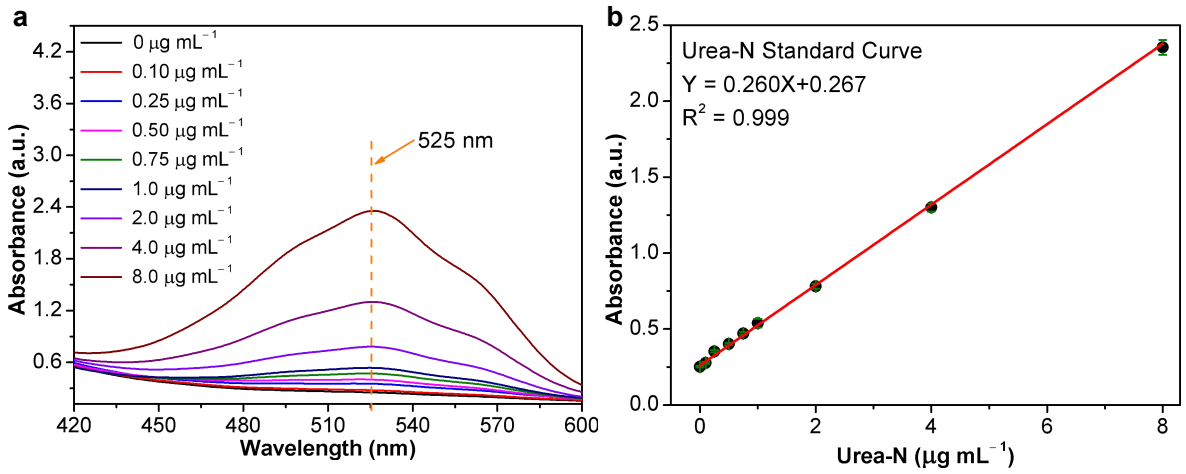

Fig. S7. (a) UV-Vis absorption spectra obtained from the solutions with different urea-N concentrations (0, 0.10, 0.25, 0.50, 0.75, 1.0, 2.0, 4.0 and 8.0 μg mL^{-1}). (b) Calibration curve used to determine urea-N concentration.

Urea standards were prepared by dissolving different amounts of urea in mixed solutions of 0.05 M KNO_3. The concentration of urea exhibits a linear relationship with the absorbance, thus the concentration of the product can be calculated *via* the fitting formula of the calibration curve.

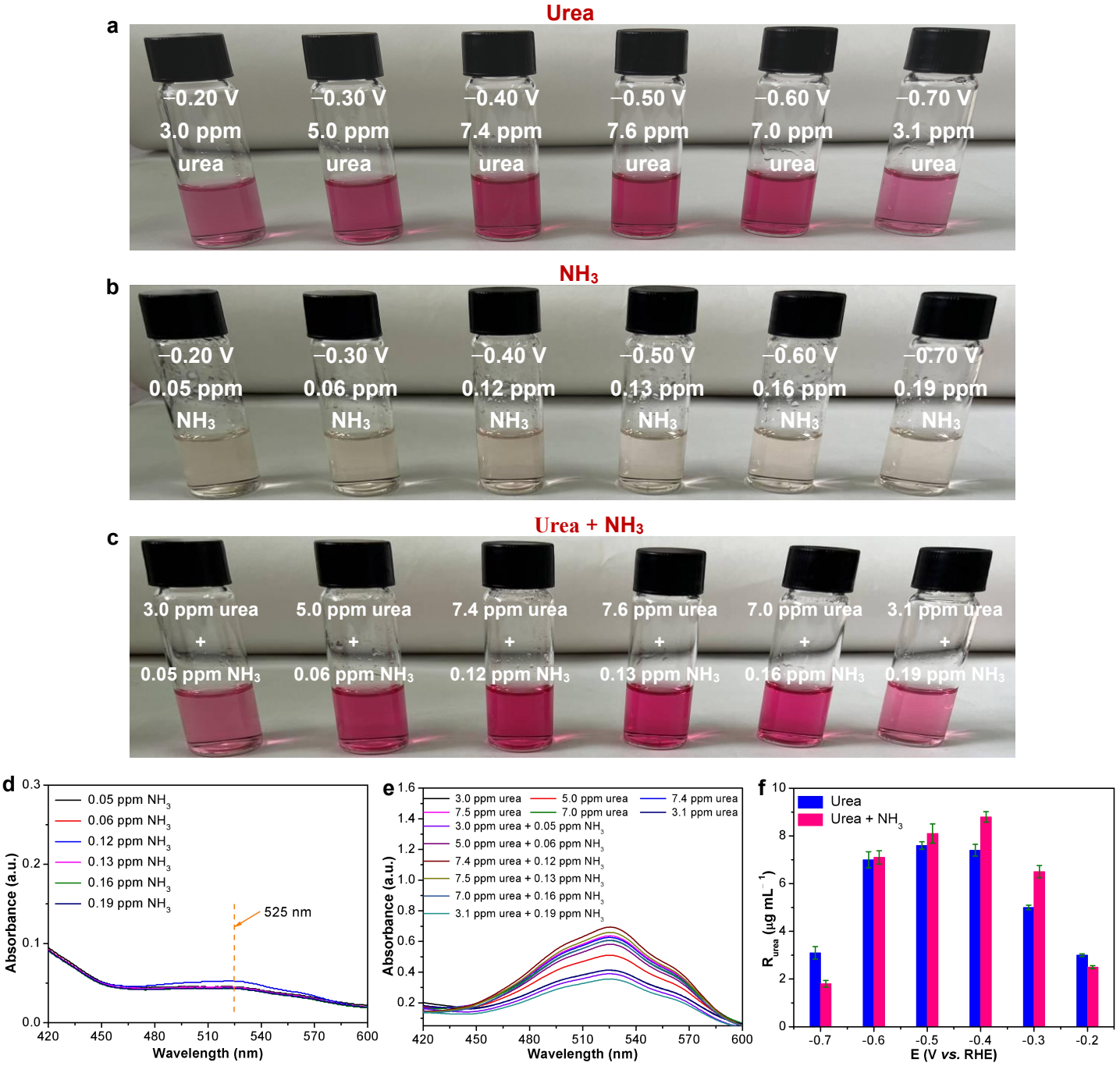

Fig. S8. Influence of coexisting NH_3 on the quantification of urea by diacetyl monoxime method. (a) Color of different concentration of urea determined by the ^1H NMR method using the data derived from Figure 2b in manuscript. (b) Color of different concentration of NH_3 determined by the indophenol blue method using the data derived from Figure S15. (c) Color of different concentration of NH_3 (derived from Figure S15) with different concentration of urea (derived from Figure 2b). (d) UV-vis absorption spectra of different concentration of NH_3 mixture solution (derived from Figure S15) quantified by diacetyl monoxime method. (e) UV-vis absorption spectra of different concentration of NH_3 (derived from Figure S15) with different concentration of urea mixture

solution (derived from Figure 2b) quantified by diacetyl monoxime method. (f) Dependence of R_{urea} of the corresponding samples.

Herein, a mixture electrolyte of 0.05 M KNO_3 was used to prepare 0.05, 0.06, 0.12, 0.13, 0.16 and 0.19 ppm NH_3 standard solution determined by the indophenol blue method using the data derived from Figure S14 and quantitatively analyzed by the diacethyl monoxime method. After color development, the results show that low concentrations of solutions NH_3 of the applied potentials also react with color regents and exhibit a light pink color (Figure S8b). The UV-vis adsorption spectra show that the maximum absorbance value at 525 nm is 0.052 corresponds to 0.12 ppm of NH_3 after diacethyl monoxime method colouration. And the intensity of adsorption peak at 525 nm gradually decreases as the NH_3 concentration further increases, which will cause false positive results for urea quantification to a certain extent (Figure S8d).

In addition, 3.0, 5.0, 7.4, 7.6, 7.0 and 3.1 ppm urea standard solution determined by the ^1H NMR method using the data derived from Figure 2b in manuscript with different concentration of NH_3 mixture solution were prepared and quantitatively analyzed by diacethyl monoxime method (Figure S8c). When there is a low concentration of NH_3 in urea solution, the color has no obvious change after color development (Figure S8a, c). However, the mixing of different concentrations of NH_3 and urea will significantly affect the absorbance (Figure S8e), and the error of urea output can reach from 1.4%−42% (Figure S8f).

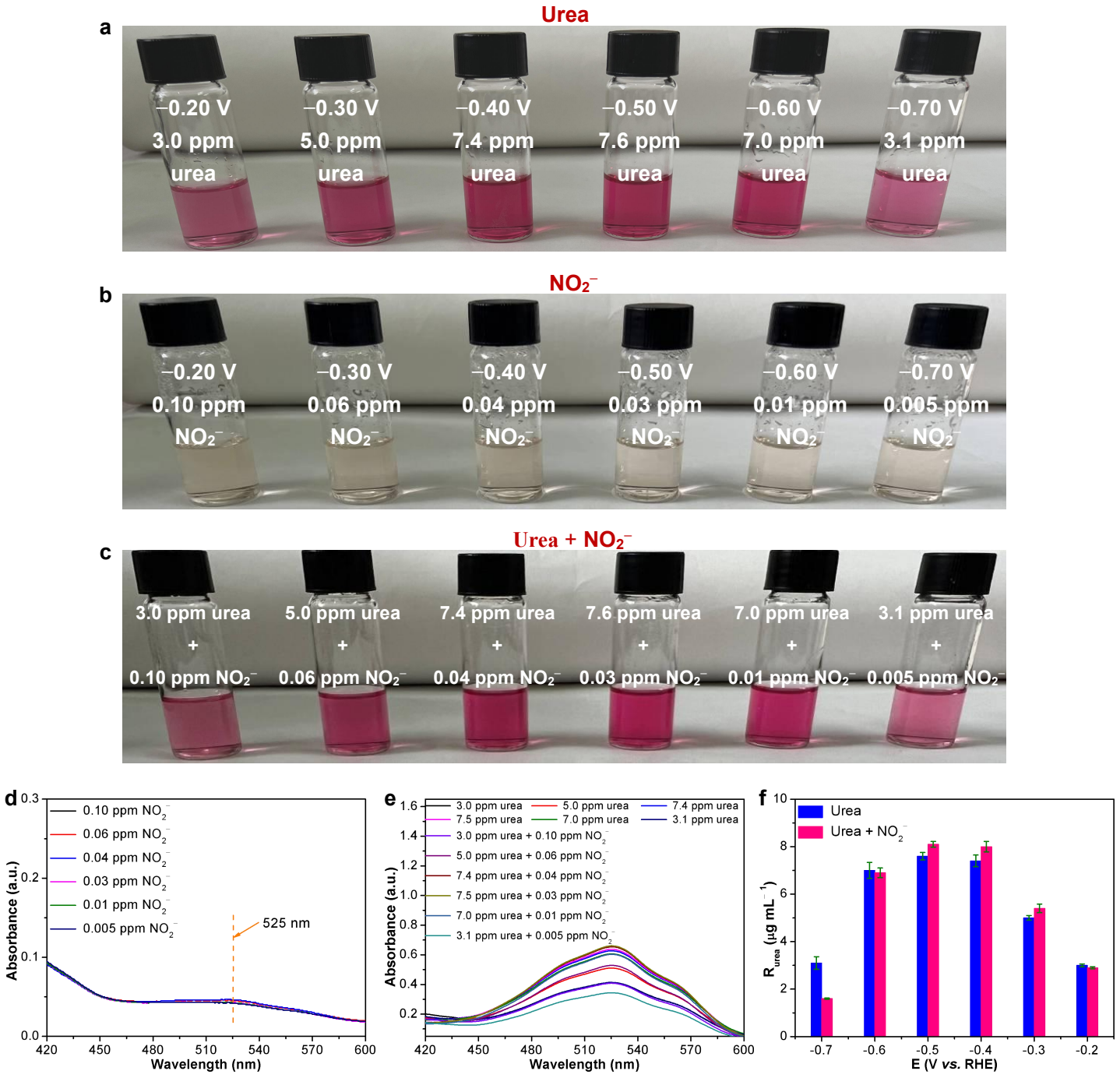

Fig. S9. Influence of coexisting NO_2^- on the quantification of urea by diacetyl monoxime method. (a) Color of different concentration of urea determined by the ^1H NMR method using the data derived from Figure 2b in manuscript. (b) Color of different concentration of NO_2^- determined by the ultraviolet spectrophotometry using the data derived from Figure S16. (c) Color of different concentration of NO_2^- (derived from Figure S16) with different concentration of urea (derived from Figure 2b). (d) UV-vis absorption spectra of different concentration of NO_2^- mixture solution (derived from Figure S16) quantified by diacetyl monoxime method. (e) UV-vis absorption spectra of different concentration of NO_2^- (derived from Figure S16) with different concentration of

urea mixture solution (derived from Figure 2b) quantified by diacetyl monoxime method. (f) Dependence of R_{urea} of the corresponding samples.

Herein, mixture electrolyte of 0.05 M KNO_3 was used to prepare 0.10, 0.06, 0.04, 0.03, 0.01 and 0.005 ppm NO_2^- standard solution determined by the ultraviolet spectrophotometry using the data derived from Figure S15 and quantitatively analyzed by diacethyl monoxime method. After color development, the results show that low concentrations of solutions NO_2^- of the applied potentials also react with color regents and exhibit a light pink color (Figure S9b). The UV-vis adsorption spectra show that all the maximum absorbance value at 525 nm is ~ 0.045 corresponds to different concentration of NO_2^- after diacethyl monoxime method colouration, which will cause false positive results for urea quantification to a certain extent (Figure S9d).

In addition, 3.0, 5.0, 7.4, 7.6, 7.0 and 3.1 ppm urea standard solution determined by the ^1H NMR method using the data derived from Figure 2b in manuscript with different concentration of NO_2^- mixture solution were prepared and quantitatively analyzed by diacethyl monoxime method (Figure S9c). When there is a low concentration of NO_2^- in urea solution, the color has no obvious change after color development (Figure S9a, c). However, the mixing of different concentrations of NO_2^- and urea will significantly affect the absorbance (Figure S9e), and the error of urea output can reach from 1.4%−48% (Figure S9f).

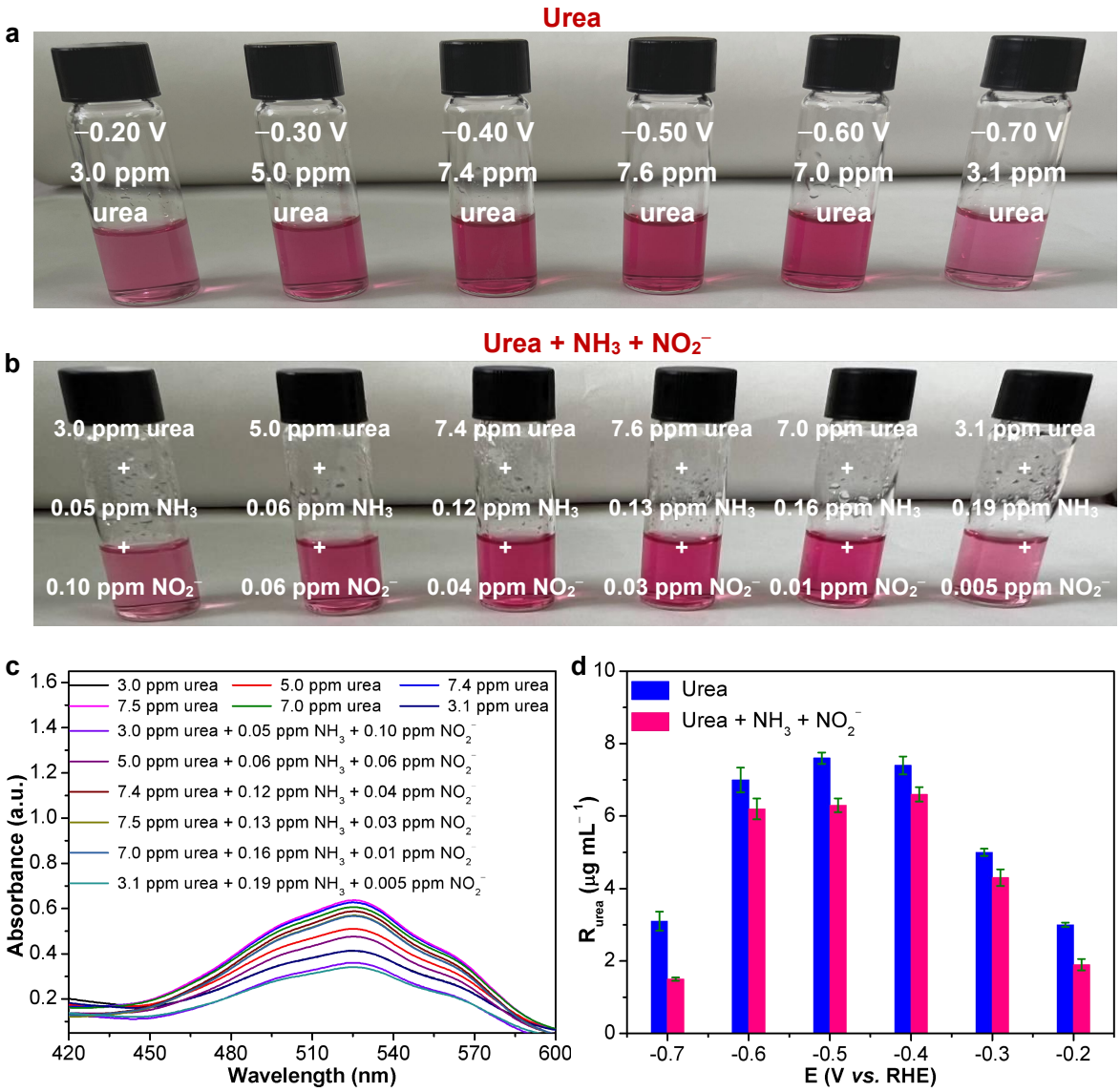

Fig. S10. Influence of coexisting NH_3 and NO_2^- on the quantification of urea by diacetyl monoxime method. (a) Color of different concentration of urea determined by the ^1H NMR method using the data derived from Figure 2b in manuscript. (b) Color of different concentration of NH_3 (derived from Figure S15) and different concentration of NO_2^- (derived from Figure S16) with different concentration of urea (derived from Figure 2b). (c) UV-vis absorption spectra of different concentration of NH_3 (derived from Figure S15) and different concentration of NO_2^- (derived from Figure S16) with different concentration of urea mixture solution (derived from Figure 2b) quantified by diacetyl monoxime method. (d) Dependence of R_{urea} of the corresponding samples.

Herein, mixture electrolyte of 0.05 M KNO_3 was used to prepare 0.05, 0.06, 0.12, 0.13,

0.16 and 0.19 ppm NH_3 standard solution determined by the indophenol blue method using the data derived from Figure S15 and 0.10, 0.06, 0.04, 0.03, 0.01 and 0.005 ppm NO_2^- standard solution determined by the ultraviolet spectrophotometry using the data derived from Figure S16 and quantitatively analyzed by diacethyl monoxime method. When there is a low concentration of NH_3 and NO_2^- in urea solution, both NH_3 and NO_2^- and urea react with color reagents. The color of all urea mixed NH_3 and NO_2^- with different concentrations is lighter than that of pure urea samples (Figure S10a, b). And the intensity of all adsorption peak at 525 nm is decrease, which will cause false positive results for urea quantification (Figure S10c). The mixing of different concentrations of NH_3, NO_2^- and urea will significantly affect the absorbance (Figure S10c), and the error of urea output can reach 10.8%−51.6% (Figure S10d).

In conclusion, the diacetyl monoxime method is mainly susceptible to interference of NH_3 and NO_2^-, both of the products of nitrate reduction, might result in the false positive results. It is not suitable for the accurate quantification of urea in coupling system of NO_3^- or NO_2^- and CO_2.

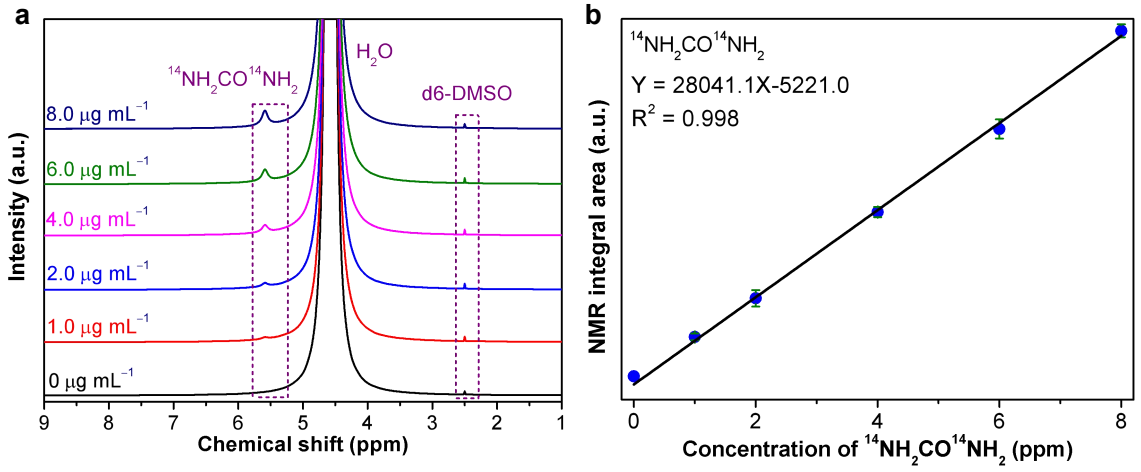

Fig. S11. (a) ^{1}H NMR spectra of $^{14}NH_2CO^{14}NH_2$ standards. (b) The corresponding $^{14}NH_2CO^{14}NH_2$ calibration curve.

Urea standards were prepared by dissolving different qualities of urea in mixed solutions of 0.05 M KNO_3. The concentration of urea exhibits a linear relationship with the integral area of characteristic peak, thus the concentration of the products could be calculated *via* the fitting formula of the calibration curves. The ^{1}H NMR spectra (Figure S11a) indicate that the $^{14}NH_2CO^{14}NH_2$ sample shows the characteristic peak at ~5.59 ppm and will not be interfered by coexisting byproducts such as NH_3 and NO_2^-.[32] The results show that ^{1}H NMR is a reliable method for the quantification of urea.

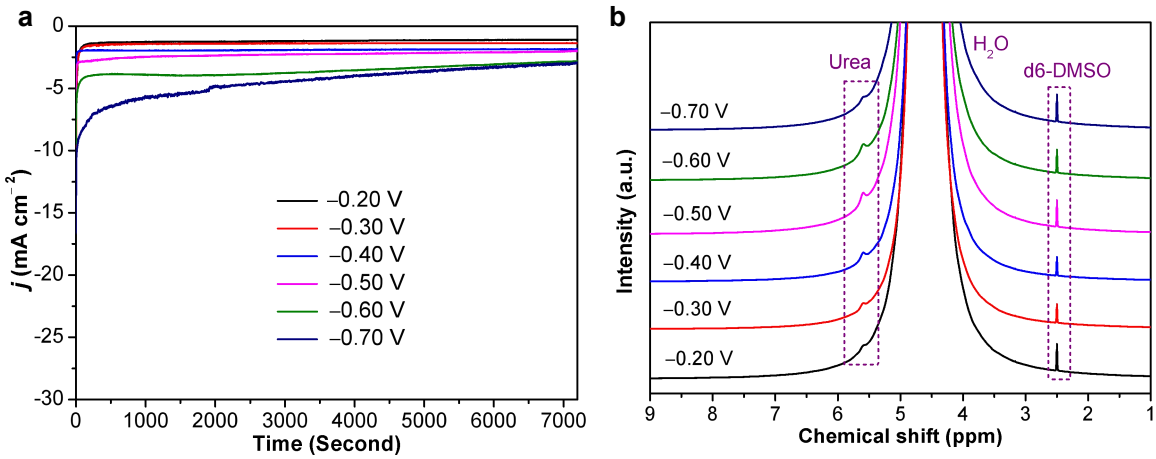

Fig. S12. (a) Time-dependent current density curves at different potentials in CO_2-saturated 0.05 M KNO_3 electrolyte over a 2 h reaction period. (b) ^1H NMR spectra of the corresponding electrolyte samples.

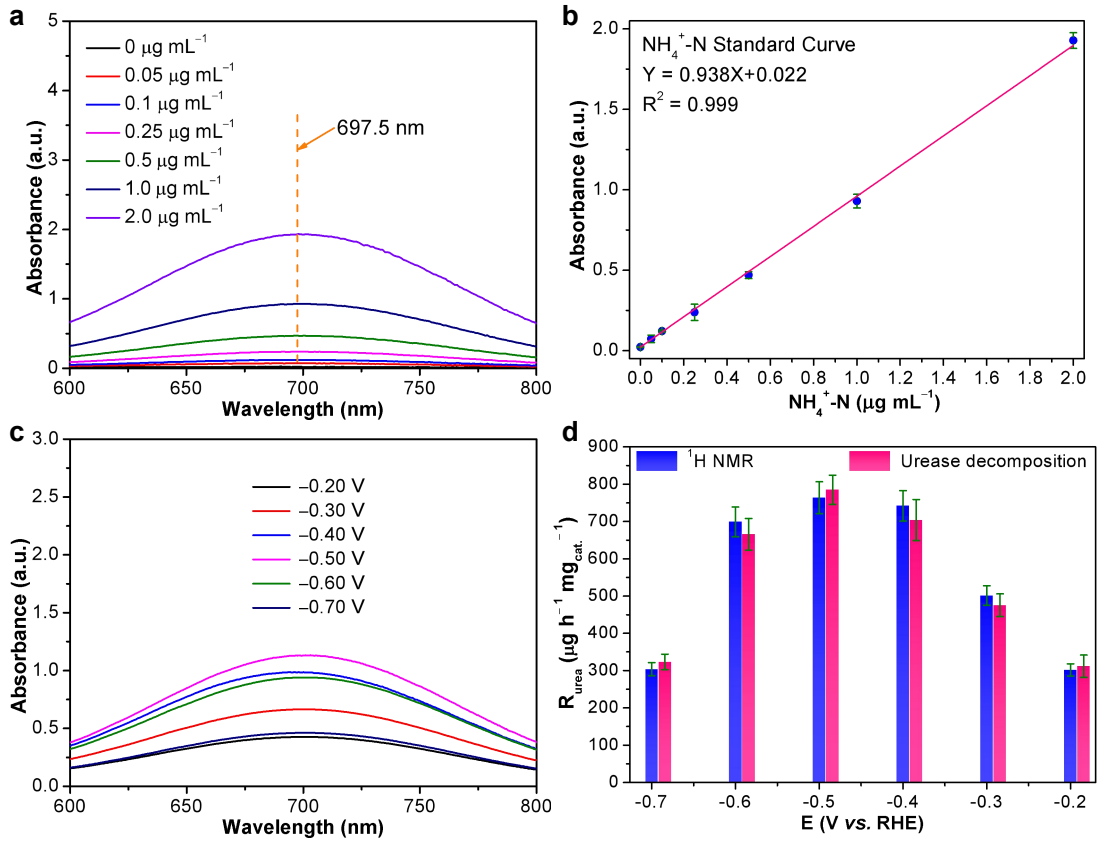

Fig. S13. (a) UV-Vis absorption spectra obtained from the solutions with different NH_4^+-N concentrations (0, 0.05, 0.10, 0.25, 0.50, 1.0 and 2.0 μg mL^{-1}). (b) Calibration curve used to determine NH_4^+-N concentration. (c) UV-Vis absorption spectra of the corresponding samples recorded in accordance with the indophenol blue method. (d) Dependence of R_{urea} on the applied potential determined using the urease decomposition and ^1H NMR methods.

For urease decomposition method, 0.4 mL of urease solution (5.0 mg mL^{-1}) was added into 3.6 mL of urea electrolyte, and then reacted at 37 °C in constant temperature shaker for 40 min. Urea was decomposed by urease into CO_2 and two NH_3 molecules. After the decomposition, NH_3 concentration of urea electrolyte with urease was detected *via* above indophenol blue method.

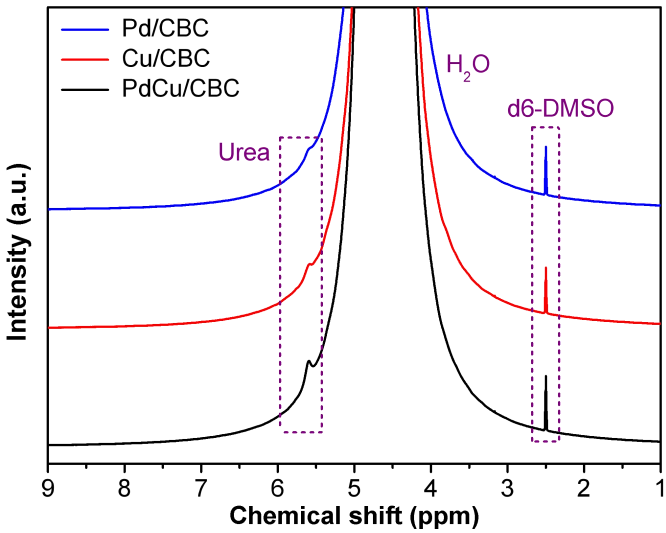

Fig. S14. ^{1}H NMR spectra of electrolyte samples obtained from Pd/CBC, Cu/CBC and PdCu/CBC catalyzed CO_2-saturated 0.05 M KNO_3 at −0.50 V (*vs.* RHE) for 2 h.

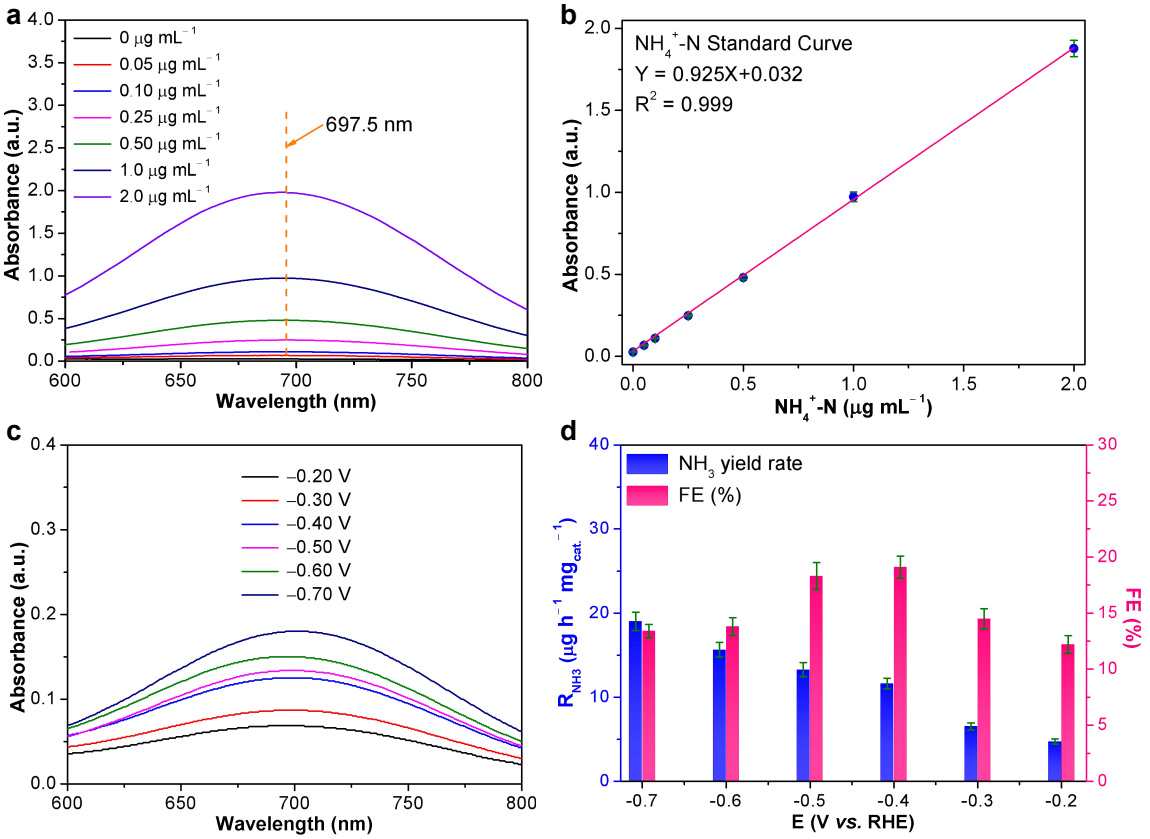

Fig. S15. (a) UV-Vis absorption spectra obtained from the solutions with different NH_4^+-N concentrations (0, 0.05, 0.10, 0.25, 0.50, 1.0 and 2.0 μg mL^{-1}). (b) Calibration curve used to determine NH_4^+-N concentration. (c) UV-Vis absorption spectra of the corresponding samples recorded in accordance with the indophenol blue method. (d) Dependence of R_{NH3} and FE on the applied potentials.

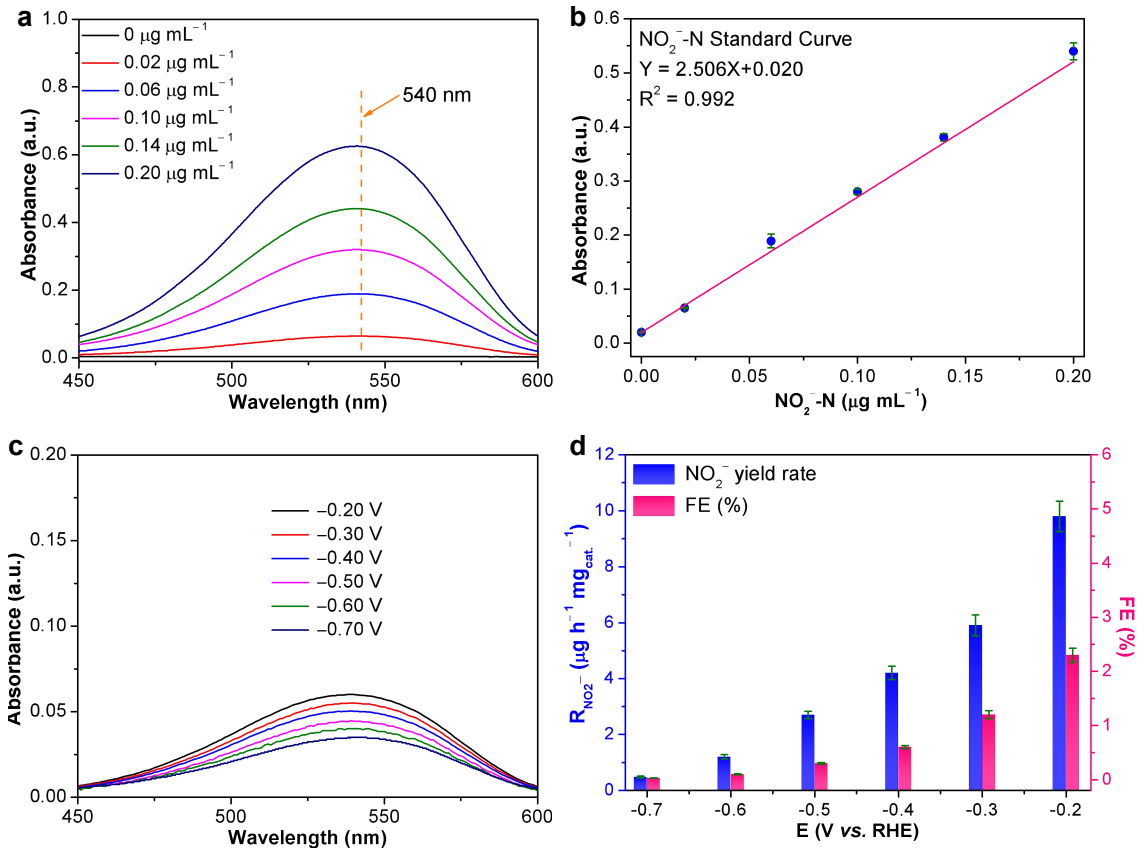

Fig. S16. (a) UV-Vis absorption spectra obtained from the solutions with different NO_2^--N concentrations (0, 0.02, 0.06, 0.10, 0.14 and 0.20 μg mL^{-1}). (b) Calibration curve used to determine NO_2^--N concentration. (c) UV-Vis absorption spectra of the corresponding samples. (d) Dependence of $R_{NO_2^-}$ and FE on the applied potentials.

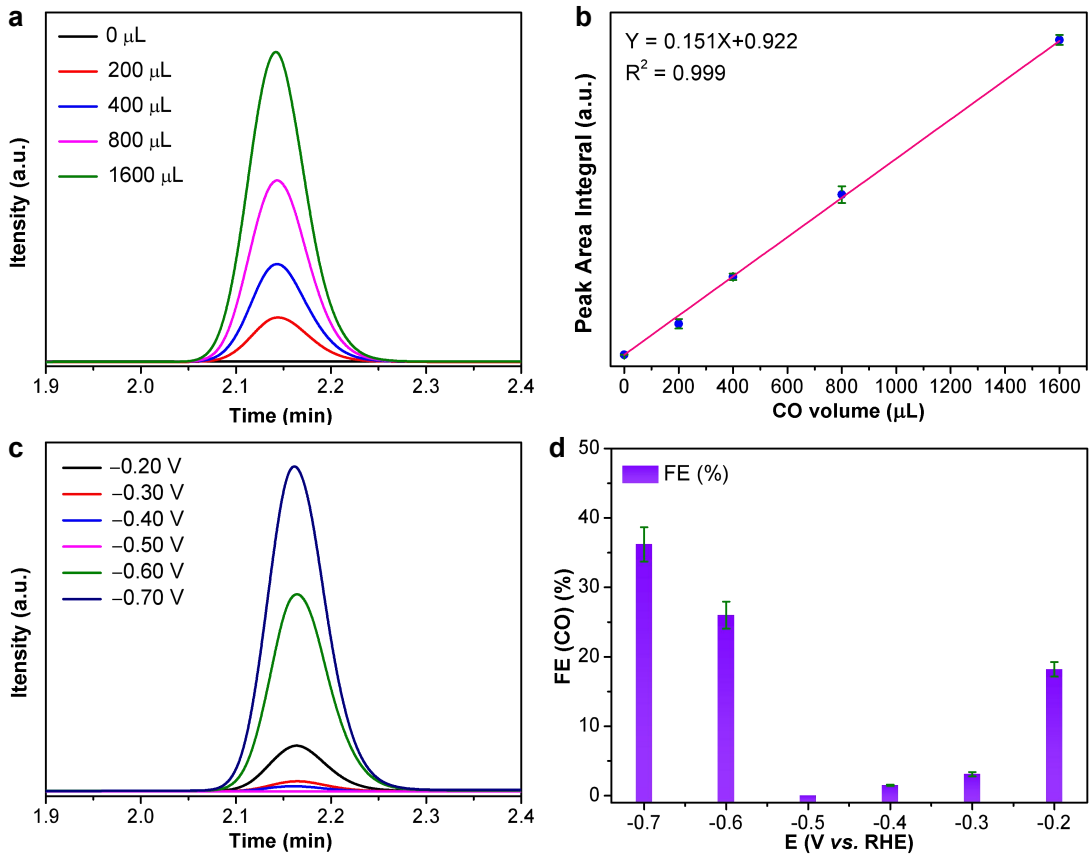

Fig. S17. Determination of CO by the gas chromatography (GC). (a) Chromatograms of the CO standards and (b) Corresponding calibration curve. (c) The chromatograms of the yielded CO resulted from PdCu/CBC catalyzed CO_2 reduction at different potentials. (d) Dependence of faradaic efficiency (FE) on the applied potential.

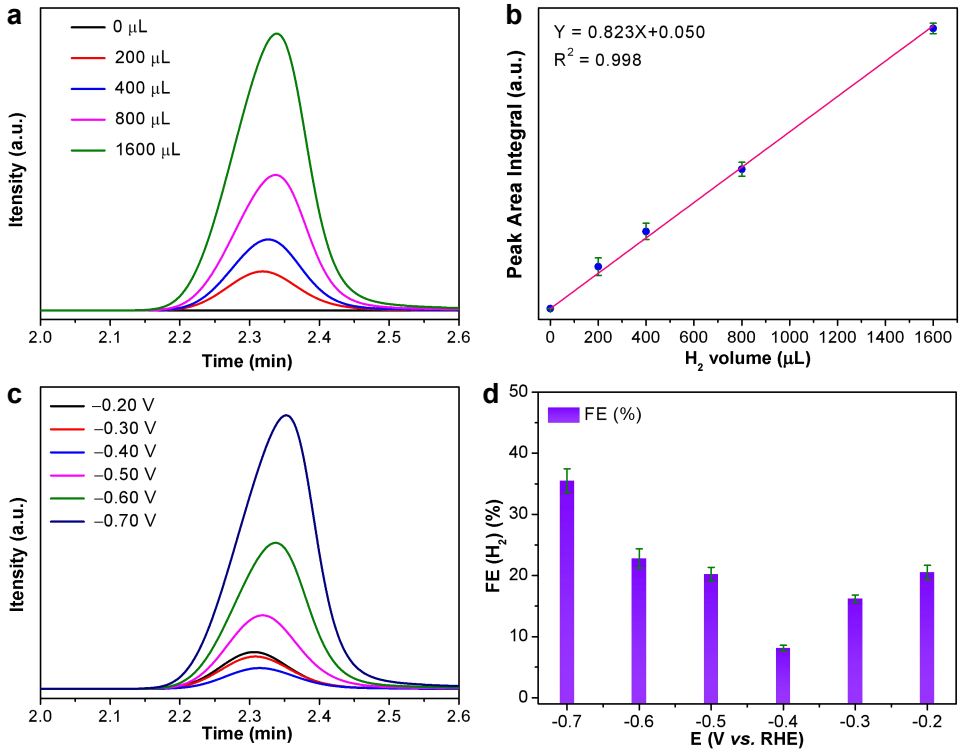

Fig. S18. Determination of H_2 by the gas chromatography (GC). (a) Chromatograms of the H_2 standards and (b) Corresponding calibration curve. (c) The chromatograms of the yielded H_2 resulted from PdCu/CBC catalyzed water decomposition at different potentials. (d) Dependence of faradaic efficiency (FE) on the applied potential.

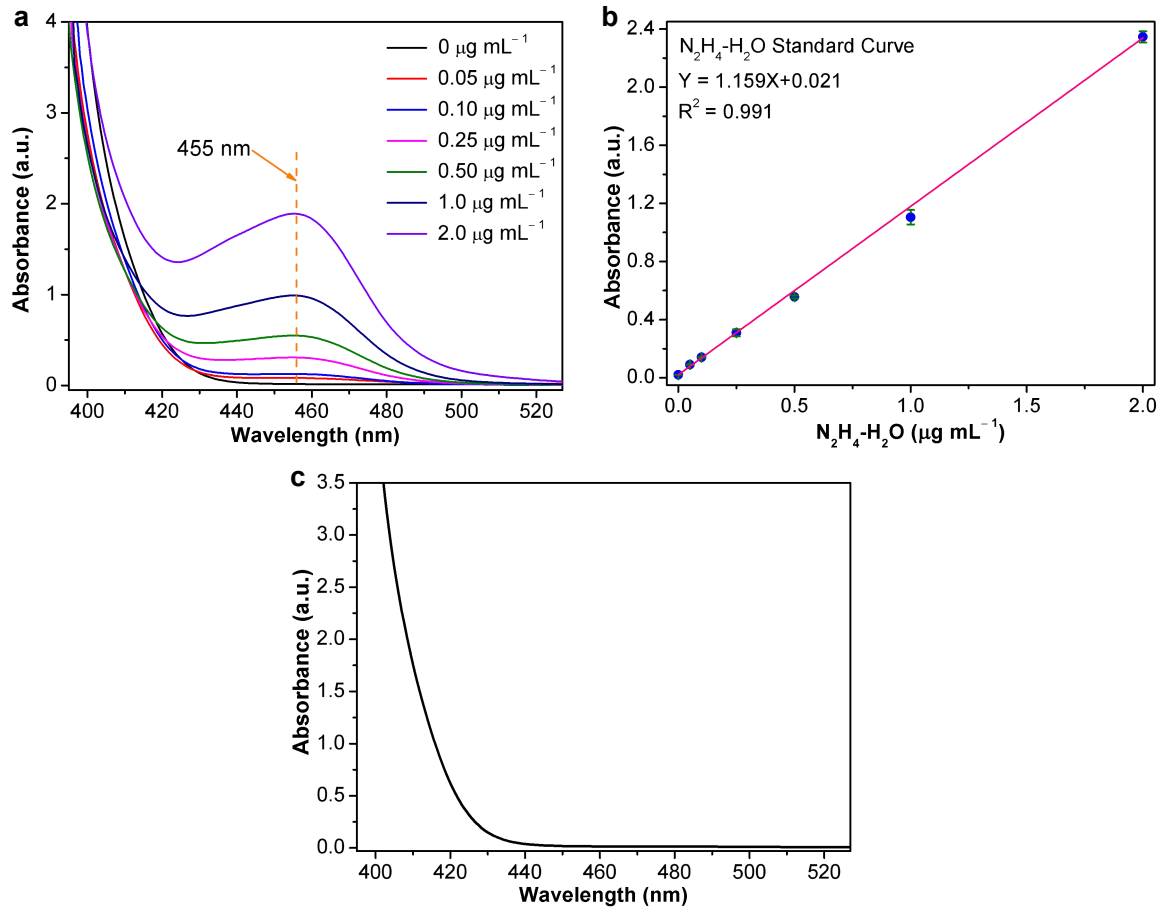

Fig. S19. Determination of $N_2H_4 \cdot H_2O$ by the Watt and Chrisp method. (a) UV-Vis absorption spectra of standard solutions containing different concentrations of $N_2H_4 \cdot H_2O$ and (b) Corresponding calibration curve. (c) UV-Vis absorption spectrum resulted from PdCu/CBC catalysed at −0.50 V (*vs.* RHE) in CO_2-saturated 0.05 M KNO_3 for 2 h coloured in accordance with Watt and Chrisp method.

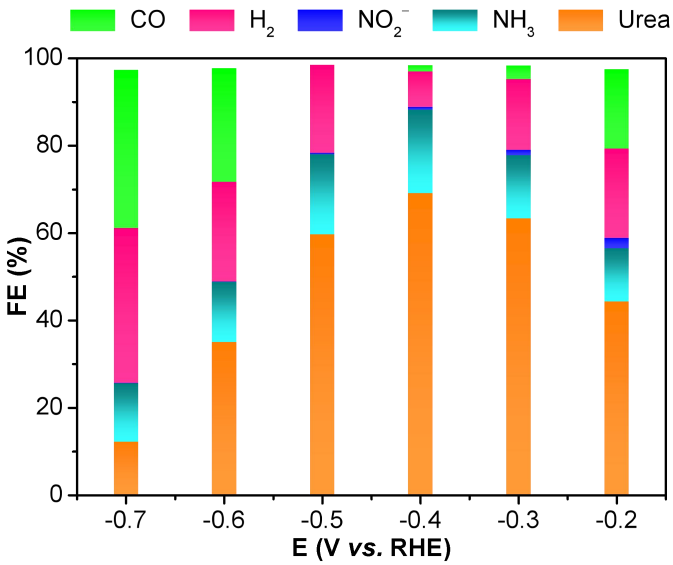

Fig. S20. FE distribution of all electrocatalytic products obtained from PdCu/CBC catalyzed urea synthesis at various potentials.

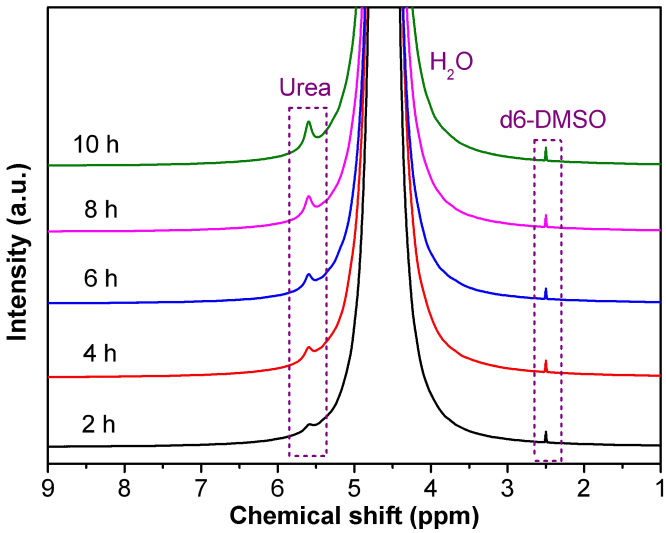

Fig. S21. ^{1}H NMR spectra of electrolyte samples obtained from PdCu/CBC toward electrochemical coupling NO_3^- with CO_2 once every 2 h with 10 h test at −0.50 V (*vs.* RHE).

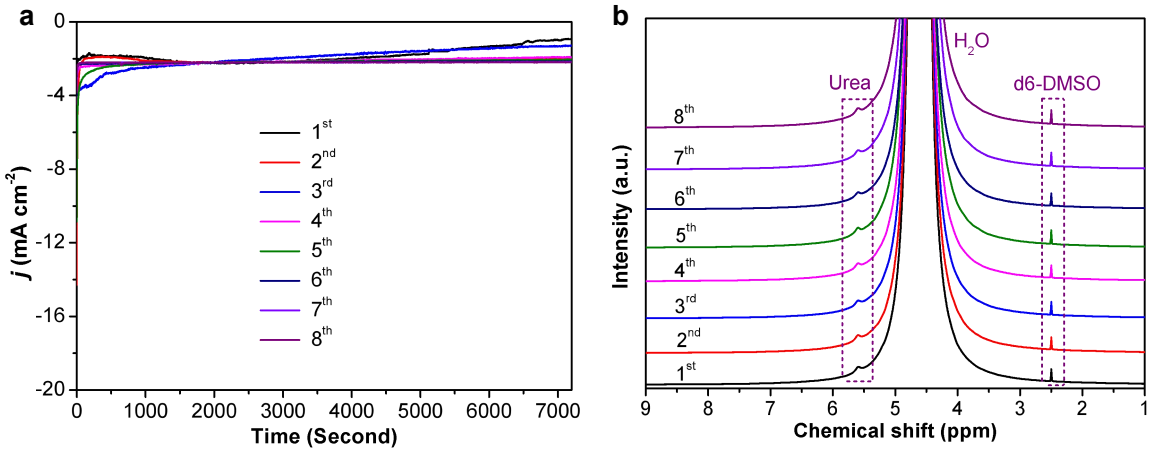

Fig. S22. (a) Cycling stability test of PdCu/CBC in CO_2-saturated 0.05 M KNO_3 electrolyte at −0.50 V (*vs.* RHE) for 8 cycles with 2 h NRR period per cycle. (b) ^1H NMR spectra of the corresponding samples.

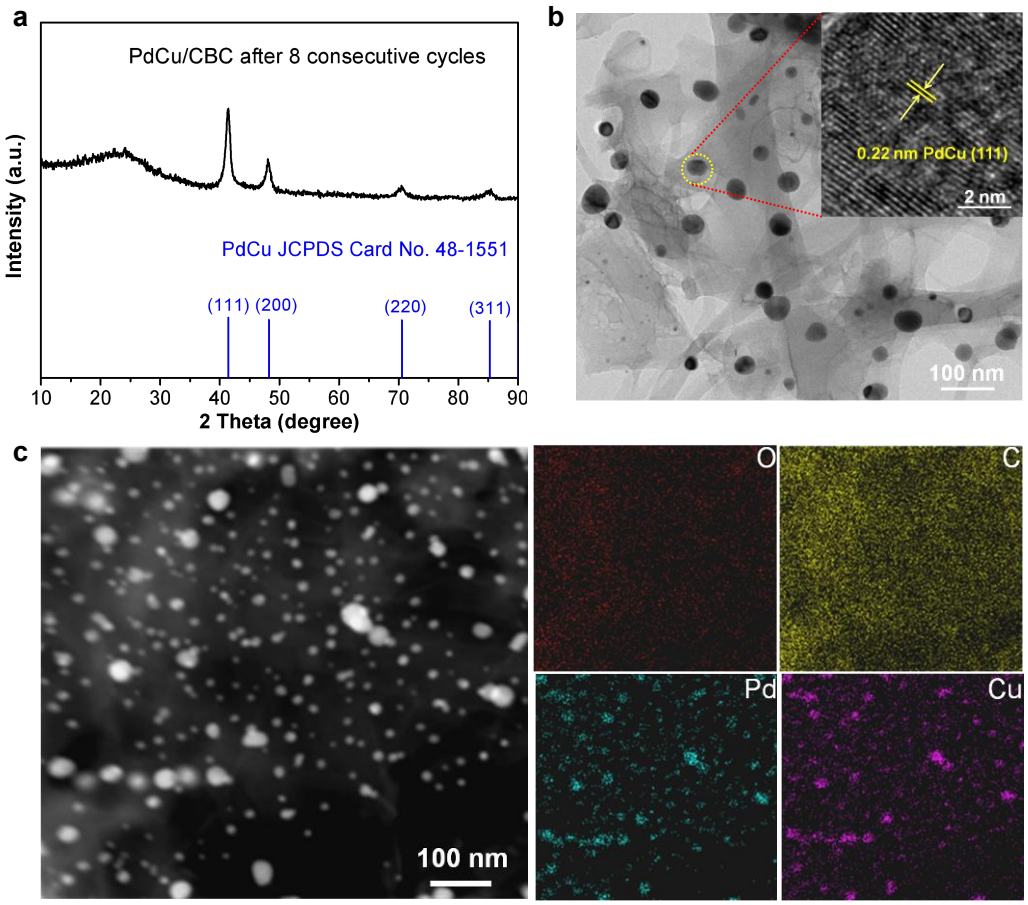

Fig. S23. (a) XRD patterns and (b) TEM images and (c) corresponding elemental mapping images of PdCu/CBC after 8 consecutive cycles.

After 8 cycles, the used PdCu/CBC catalyst still exhibits that PdCu alloy form. The XRD, TEM and corresponding elemental mapping results unequivocally indicate that PdCu alloy catalyst possesses good structure stability.

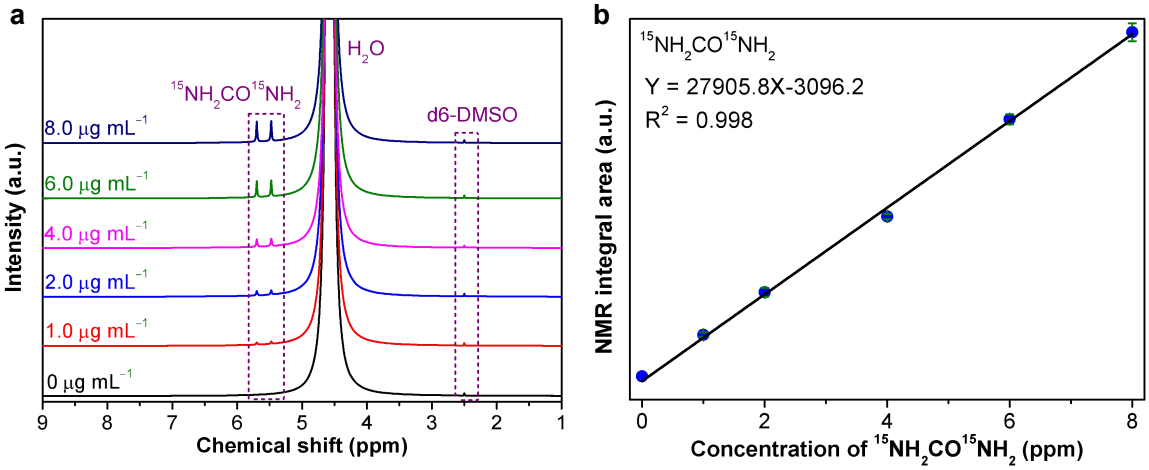

Fig. S24. (a) ^{1}H NMR spectra of $^{15}NH_2CO^{15}NH_2$ standards. (b) The corresponding $^{15}NH_2CO^{15}NH_2$ calibration curve.

Urea standards were prepared by dissolving different qualities of urea in mixed solutions of 0.05 M $K^{15}NO_3$. The concentration of urea exhibits a linear relationship with the integral area of characteristic peak, thus the concentration of the products could be calculated *via* the fitting formula of the calibration curves.

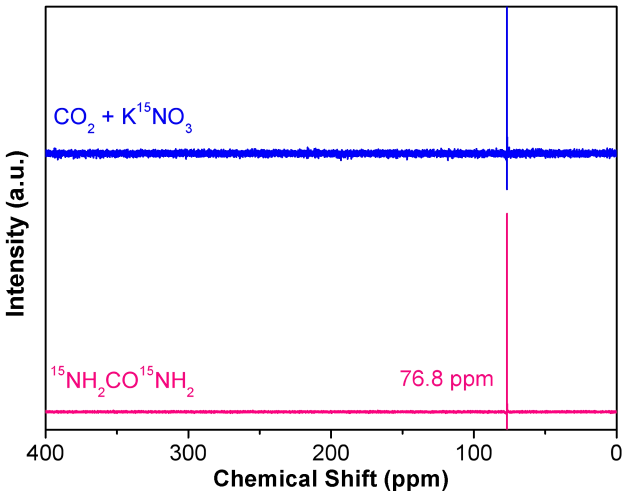

Fig. S25. ^{15}N NMR spectra of 0.05 M $^{15}KNO_3$ electrolytes saturated with CO_2 after 2 h of electrolysis and standard $^{15}NH_2CO^{15}NH_2$ solutions.

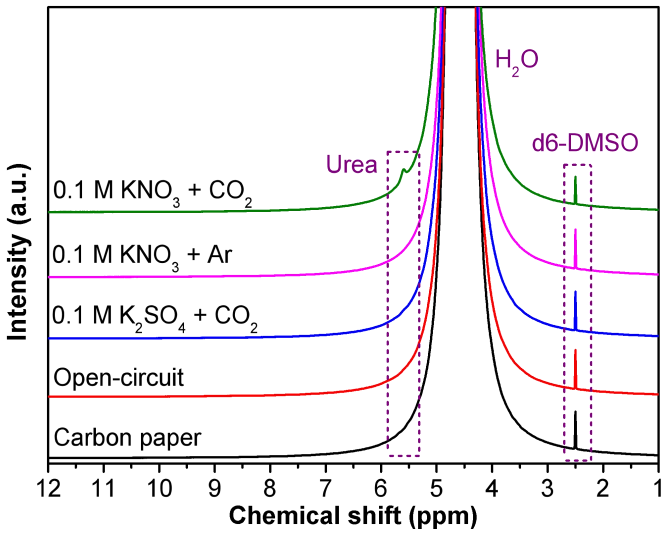

Fig. S26. ^{1}H NMR spectra of the samples obtained at different conditions.

^{1}H NMR spectra of the CO_2-saturated 0.05 M KNO_3, Ar-saturated 0.05 M KNO_3, CO_2-saturated 0.05 M KNO_3 without applied potential (Open-circuit), CO_2-saturated 0.05 M K_2SO_4 without any nitrogen-containing precursor, carbon paper without PdCu/CBC electrocatalyst under −0.50 V *vs.* RHE for 2 h.

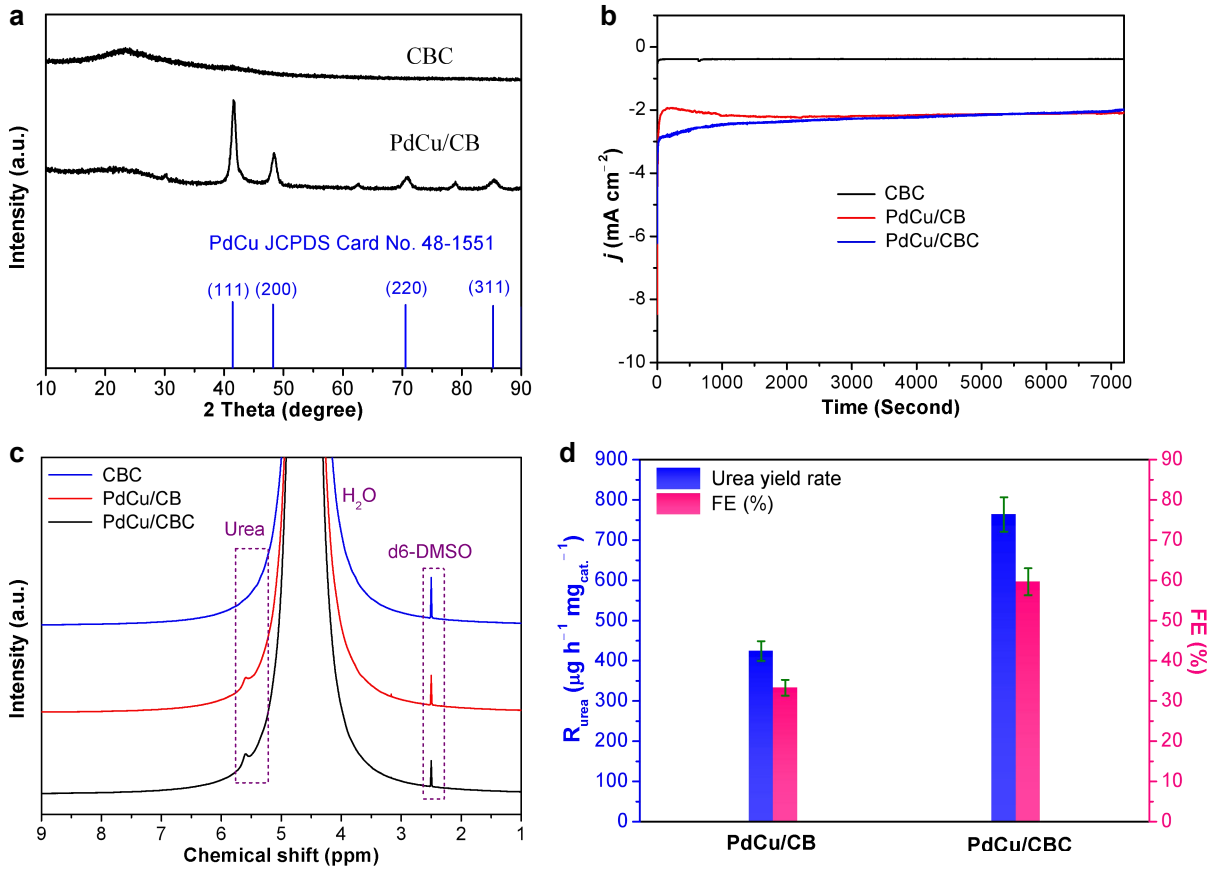

Fig. S27. (a) XRD patterns of CBC and PdCu/CB. (b) Time-dependent current density curves of CBC, PdCu/CBC and PdCu/CB at −0.50 V (*vs.* RHE) in CO_2-saturated 0.05 M KNO_3 for 2 h. (c) ^{1}H NMR spectra of the CBC, PdCu/CB and PdCu/CBC samples catalysed at −0.50 V (*vs.* RHE) in CO_2-saturated 0.05 M KNO_3 for 2 h. (d) Dependence of R_{urea} and FE of PdCu/CBC and PdCu/CB determined using the ^{1}H NMR methods.

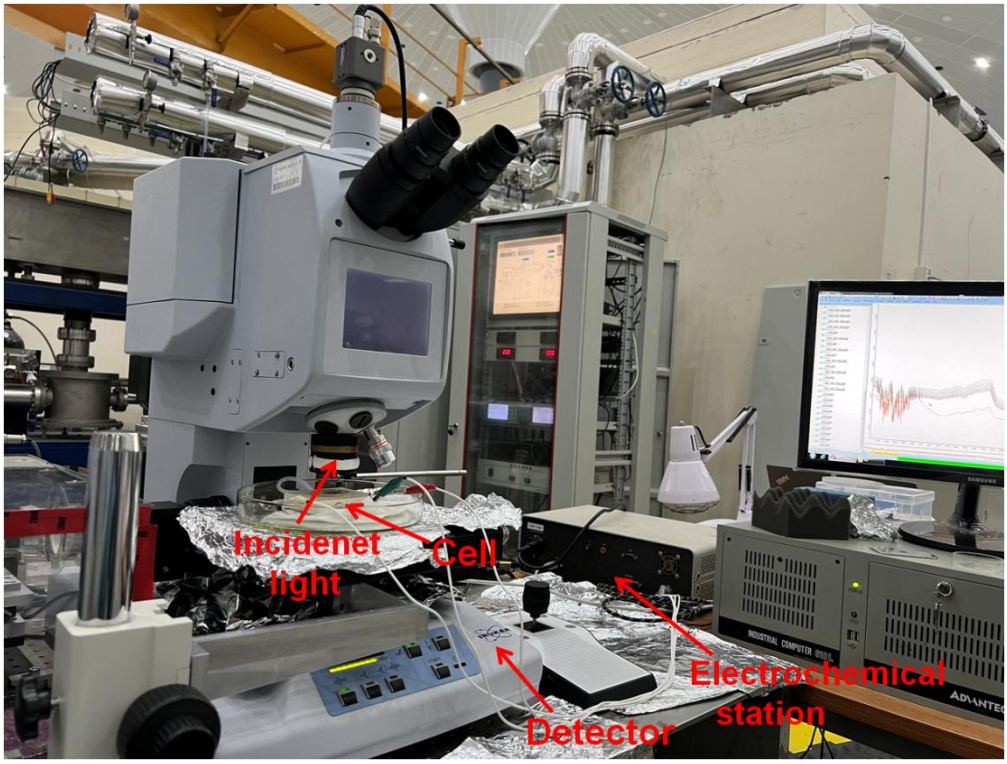

Fig. S28. The experimental setup for the *Operando* synchrotron radiation FTIR measurements.

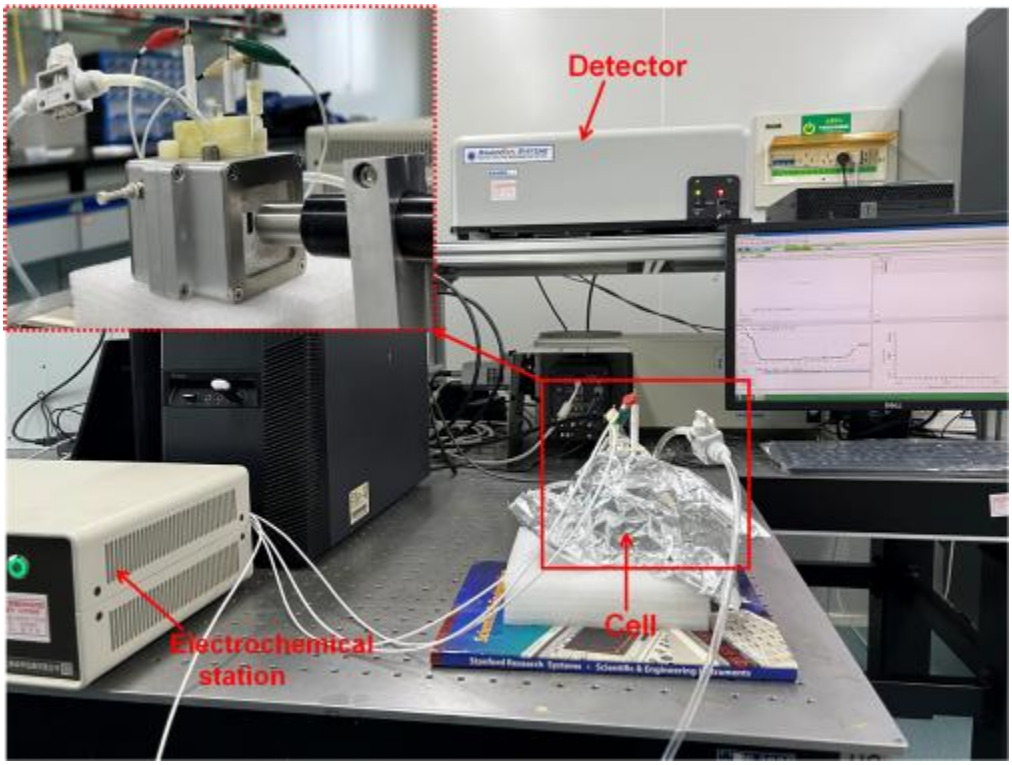

Fig. S29. The experimental setup for the *Operando* Raman measurements.

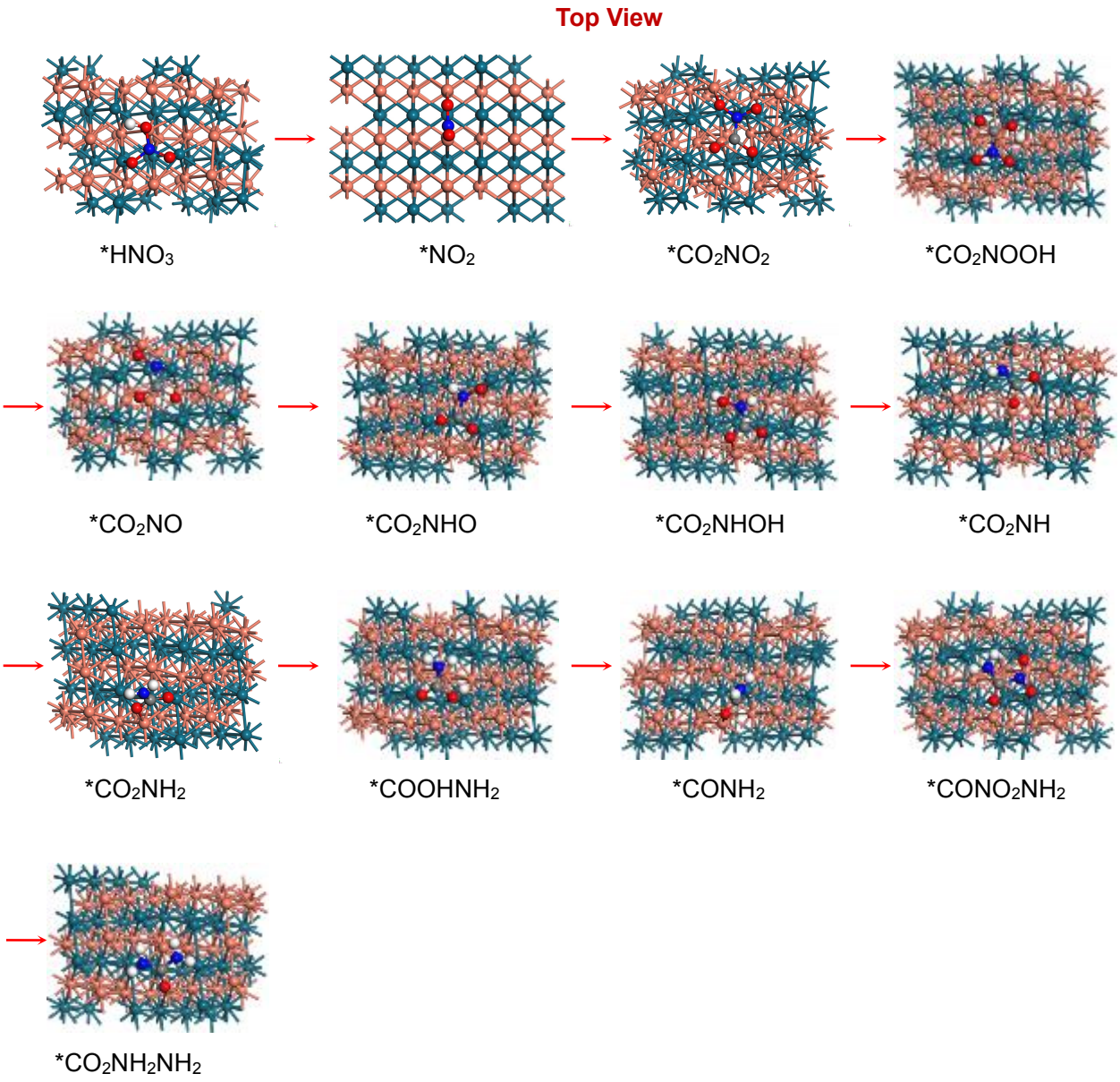

Fig. S30. Top view of corresponding intermediates structures for each step. The green, orange, blue, red, white and grey balls represent Pd, Cu, N, O, H and C atoms, respectively.

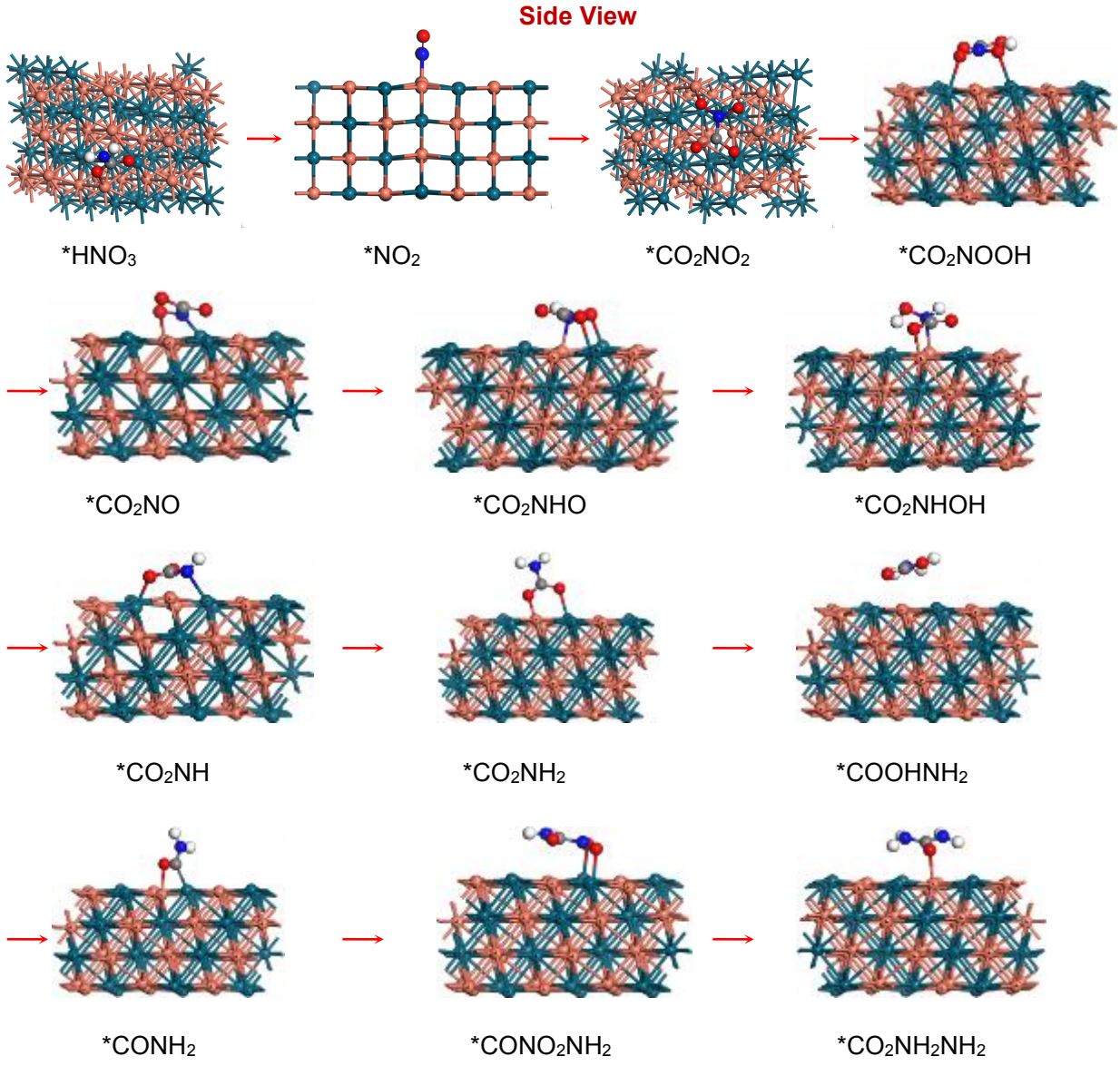

Fig. S31. Side view of corresponding intermediates structures for each step. The green, orange, blue, red, white and grey balls represent Pd, Cu, N, O, H and C atoms, respectively.

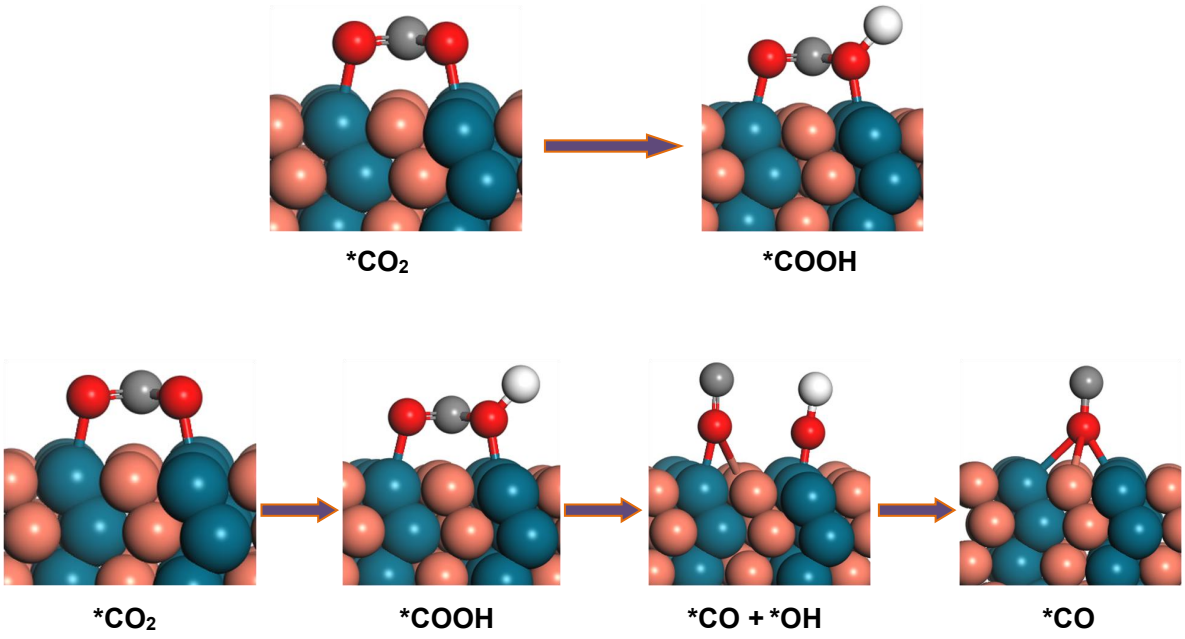

Fig. S32. Corresponding intermediates structures of *CO_2 to *COOH and *COOH to *CO + *OH reaction pathways on PdCu (111) plane. The green, orange, blue, red, white and grey balls represent Pd, Cu, N, O, H and C atoms, respectively.

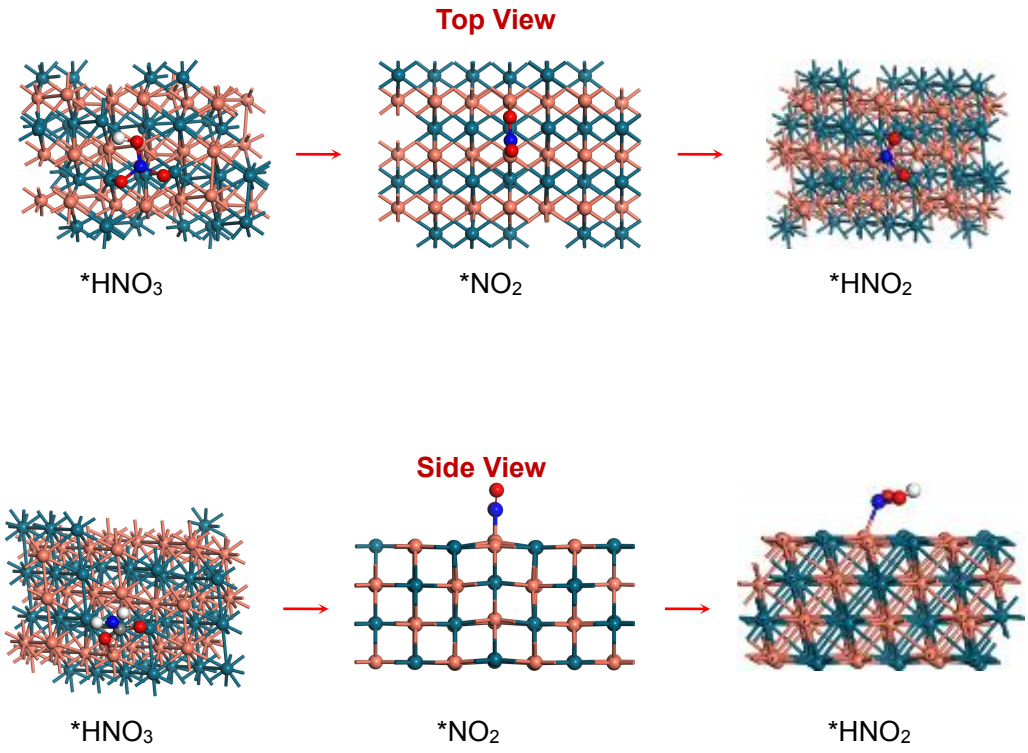

Fig. S33. Top view and side view of corresponding intermediates structures for each step. The green, orange, blue, red and white balls represent Pd, Cu, N, O and H atoms, respectively.

References

1 C. Lv, L. Zhong, H. Liu, Z. Fang, C. Yan, M. Chen, Y. Kong, C. Lee, D. Liu and S. Li, *Nat. Sustain.*, 2021, **4**, 868-876.

2 L. Liu, H. Mo, S. Wei and D. Raftery, *Analyst*, 2012, **137**, 595-600.

3 X. Wei, X. Wen, Y. Liu, C. Chen, C. Xie, D. Wang, M. Qiu, N. He, P. Zhou, W. Chen, J. Cheng, H. Lin, J. Jia, X.-Z. Fu and S. Wang, *J. Am. Chem. Soc.*, 2022, **144**, 11530-11535.

4 Q. Gao, H. S. Pillai, Y. Huang, S. Liu, Q. Mu, X. Han, Z. Yan, H. Zhou, Q. He, H. Xin and H. Zhu, *Nat. Commun.*, 2022, **13**, 2338.

5 S. Zhang, T. Shi, K. Li, Q. Sun, Y. Lin, L. R. Zheng, G. Wang, Y. Zhang, H. Yin and H. Zhang, *J. Phys. Chem. C*, 2022, **126**, 965-973.

6 S. Zhang, M. Jin, T. Shi, M. Han, Q. Sun, Y. Lin, Z. Ding, L. R. Zheng, G. Wang and Y. Zhang, *Angew. Chem., Int. Ed.*, 2020, **59**, 13423-13429.

7 G. Kresse and D. Joubert, *Phys. Rev. B*, 1999, **59**, 1758.

8 J. J. Mortensen, L. B. Hansen and K. W. Jacobsen, *Phys. Rev. B*, 2005, **71**, 035109.

9 J. Perdew, K. Burke and M. Ernzerhof, *Phys. Rev. Lett*, 1998, **80**, 891.

10 J. P. Perdew, J. Chevary, S. Vosko, K. A. Jackson, M. R. Pederson, D. Singh and C. Fiolhais, *Phys. Rev. B*, 1993, **48**, 4978.

11 J. K. Nørskov, J. Rossmeisl, A. Logadottir, L. Lindqvist, J. R. Kitchin, T. Bligaard and H. Jonsson, *J. Phys. Chem. B*, 2004, **108**, 17886-17892.

12 C. Chen, X. Zhu, X. Wen, Y. Zhou, L. Zhou, H. Li, L. Tao, Q. Li, S. Du, T. Liu, D. Yan, C. Xie, Y. Zou, Y. Wang, R. Chen, J. Huo, Y. Li, J. Cheng, H. Su, X. Zhao, W. Cheng, Q. Liu, H. Lin, J. Luo, J. Chen, M. Dong, K. Cheng, C. Li and S. Wang, *Nat. Chem.*, 2020, **12**, 717-724.

13 D. B. Kayan and F. Köleli, *Appl. Catal. B: Environ.*, 2016, **181**, 88-93.

14 M. Yuan, J. Chen, Y. Bai, Z. Liu, J. Zhang, T. Zhao, Q. Wang, S. Li, H. He and G. Zhang, *Angew. Chem., Int. Ed.*, 2021, **60**, 10910-10918.

15 M. Yuan, J. Chen, Y. Bai, Z. Liu, J. Zhang, T. Zhao, Q. Shi, S. Li, X. Wang and G. Zhang, *Chem. Sci.*, 2021, **12**, 6048-6058.

16 M. Yuan, J. Chen, Y. Xu, R. Liu, T. Zhao, J. Zhang, Z. Ren, Z. Liu, C. Streb, H. He, C. Yang, S. Zhang and G. Zhang, *Energy Environ. Sci.*, 2021, **14**, 6605-6615.

17 M. Yuan, J. Chen, H. Zhang, Q. Li, L. Zhou, C. Yang, R. Liu, Z. Liu, S. Zhang and G. Zhang, *Energy Environ. Sci.*, 2022, **15**, 2084-2095.

18 M. Yuan, H. Zhang, Y. Xu, R. Liu, R. Wang, T. Zhao, J. Zhang, Z. Liu, H. He, C. Yang, S. Zhang and G. Zhang, *Chem Catal.*, 2022, **2**, 309-3207.

19 M. Shibata and N. Furuya, *J. Electroanal. Chem.*, 2001, **507**, 177-184.

20 P. Siva, P. Prabu, M. Selvam, S. Karthik and V. Rajendran, *Ionics*, 2017, **23**, 1871-1878.

21 N. Cao, Y. Quan, A. Guan, C. Yang, Y. Ji, L. Zhang and G. Zheng, *J. Colloid Interf. Sci.*, 2020, **577**, 109-114.

22 Y. Feng, H. Yang, Y. Zhang, X. Huang, L. Li, T. Cheng and Q. Shao, *Nano Lett.*, 2020, **20**, 8282-8289.

23 S. Liu, S. Yin, Z. Wang, Y. Xu, X. Li, L. Wang and H. Wang, *Cell Rep. Phys. Sci.*, 2022, **3**, 100869.

24 N. Meng, Y. Huang, Y. Liu, Y. Yu and B. Zhang, *Cell Rep. Phys. Sci.*, 2021, **2**, 100378.

25 Y. Huang, R. Yang, C. Wang, N. Meng, Y. Shi, Y. Yu and B. Zhang, *ACS Energy Lett.*, 2022, **7**, 284-291.

26 M. Shibata, K. Yoshida and N. Furuya, *J. Electroanal. Chem.*, 1995, **387**, 143-145.

27 D. Saravanakumar, J. Song, S. Lee, N. H. Hur and W. Shin, *ChemSusChem*, 2017, **10**, 3999-4003.

28 C. Lv, C. Lee, L. Zhong, H. Liu, J. Liu, L. Yang, C. Yan, W. Yu, H. H. Hng, Z. Qi, L. Song, S. Li, K. P. Loh, Q. Yan and G. Yu, *ACS Nano*, 2022, **16**, 8213-8222.

29 N. Meng, X. Ma, C. Wang, Y. Wang, R. Yang, J. Shao, Y. Huang, Y. Xu, B. Zhang and Y. Yu, *ACS Nano*, 2022, **16**, 9095-9104.

30 J. Leverett, T. Tran-Phu, J. A. Yuwono, P. Kumar, C. Kim, Q. Zhai, C. Han, J. Qu, J. Cairney, A. N. Simonov, R. K. Hocking, L. Dai, R. Daiyan and R. Amal, *Adv. Energy Mater.*, 2022, 2201500. https://doi.org/10.1002/aenm.202201500.

31 X. Liu, P. V. Kumar, Q. Chen, L. Zhao, F. Ye, X. Ma, D. Liu, X. Chen, L. Dai and C. Hu, *Appl. Catal. B: Environ.*, 2022, **316**, 121618.

32 X. Zhang, X. Zhu, S. Bo, C. Chen, M. Qiu, X. Wei, N. He, C. Xie, W. Chen and J. Zheng, *Nat. Commun.*, 2022, **13**, 1.